



Constraining the Hydrogen Soil Sink and Photochemical Source: Insights from Atmospheric H₂ Inversions (2003–2023)

Firmin T. Stroo¹, Joram J. D. Hooghiem², Maarten C. Krol^{2,3}, and Wouter Peters²

¹Centre for Isotope Research (CIO), Energy and Sustainability Research Institute Groningen (ESRIG) at University of Groningen, Groningen, The Netherlands

²Department of Meteorology and Air Quality at Wageningen University & Research, Wageningen, The Netherlands

³Institute for Marine and Atmospheric Research Utrecht at Utrecht University, Utrecht, The Netherlands

Correspondence: Firmin T. Stroo (f.t.stroo@rug.nl)

Abstract. Hydrogen (H₂) is expected to become an increasingly important energy carrier during the energy transition, likely leading to higher atmospheric H₂ levels due to losses during production, transport, storage and usage of hydrogen. Multiple studies have shown this could impact atmospheric composition through interactions with the hydroxyl radical. However, the magnitude of this impact remains uncertain due to large uncertainties in the global H₂ budget, particularly in the soil sink and photochemical source. To address this, we present a spatiotemporally resolved H₂ budget derived using atmospheric inversions with the TM5 chemical transport model. With this approach, we infer a global mean soil sink of 52.8 [47.8–56.7] Tg yr⁻¹ and a photochemical source of 34.6 [29.2–38.2] Tg yr⁻¹ over 2003–2023. Relative to Ouyang et al. (2025), we estimate a soil sink that is 45% and 35% weaker in the Middle East and Oceania, and 45% and 70% stronger in South America and Russia, respectively. Our results further suggest that variability in the observed H₂ growth rate between 2003–2023 was primarily driven by changes in the photochemical source from CH₄ oxidation, together with a declining global soil sink at a mean rate of 0.23 Tg yr⁻². Finally, we infer a sensitivity of the soil sink to the El Niño–Southern Oscillation, strongest over diffusion-limited soils in tropical South America, with increased uptake during drier El Niño conditions and reduced uptake during wetter La Niña conditions.

1 Introduction

Global hydrogen (H₂) demand has roughly doubled over the last two decades and is projected to keep increasing during the ongoing energy transition (IEA, 2019, 2023). As a result, atmospheric H₂ levels may increase due to unavoidable losses across production, transport, storage, and usage of hydrogen (De Kleijne et al., 2024; Ocko and Hamburg, 2022). This could impact tropospheric methane (CH₄) and ozone (O₃), as well as stratospheric water vapour levels, through interactions with the hydroxyl radical (OH). Together, these effects yield a 100-year global warming potential (GWP₁₀₀) for hydrogen of 11.6 ± 2.8 (Sand et al., 2023), meaning that 1 kg of H₂ emitted has a climate impact equivalent to 11.6 ± 2.8 kg of CO₂ emitted over a 100-year horizon. The uncertainty in the GWP₁₀₀ estimate arises primarily from a limited understanding of the global hydrogen budget. Particularly, the photochemical H₂ source and the soil sink, representing the two largest fluxes in the budget, are highly uncertain. According to the recent comprehensive assessment of the global H₂ budget by Ouyang et al. (2025),



the remaining terms in the budget, including biomass burning, fossil fuel combustion, ocean emissions, land emissions from
25 N₂ fixing bacteria, and the OH sink, are comparatively well constrained in magnitude. This study provides the most detailed
uncertainty assessment of the global hydrogen budget to date, based on a diverse ensemble of bottom-up approaches, and will
therefore be referred to frequently throughout the remainder of this paper.

The global photochemical H₂ source from formaldehyde (CH₂O) photolysis is the most uncertain source in the H₂ bud-
get. It arises from multiple pathways reflecting the diversity of CH₂O precursors and is typically quantified using global
30 chemical transport model simulations. The contribution from CH₄ oxidation, the dominant precursor pathway via CH₂O, is
relatively well constrained. This is because CH₄ is a long-lived greenhouse gas with well-characterised global atmospheric
abundances, constrained by extensive surface and satellite observations. In contrast, the contribution from oxidation of anthro-
pogenic and biogenic Volatile Organic Compounds (VOCs) is more uncertain, reflecting shorter atmospheric lifetimes and less
well-constrained emission inventories of these precursors.

35 The global H₂ soil sink is the largest and most uncertain term in the H₂ budget (Sand et al., 2026). Its uncertainty arises from
a complex dependence on multiple interacting environmental drivers, including soil moisture, soil temperature, and soil organic
carbon content. It also exhibits strong spatial variability, with field measurements showing that fluxes can differ substantially
between sites only a few kilometres apart (Cowan et al., 2025). Estimates of the global H₂ soil sink rely on parametrisations
predominantly derived from field measurements at mid-latitude Northern Hemisphere sites (Ehhalt and Rohrer, 2009). This
40 introduces a representativeness bias, since tropical regions, expected to exhibit the highest uptake rates (Tardito Chaudhri and
Stevenson, 2025), are not represented in the underlying observations. In addition, parametrisations are limited by the lack of
accurate, high-resolution forcing data for key drivers such as soil moisture and soil temperature, further introducing uncertainty
in global flux estimates. Finally, a key limitation of most bottom-up studies is that their fluxes are not propagated through three-
dimensional transport models, making it impossible to verify their consistency with long-term global H₂ observations.

45 To overcome some of these challenges, a top-down approach can be used. Here, bottom-up fluxes serve as a first guess and
are subsequently adjusted using H₂ mole fraction measurements. These atmospheric observations integrate information from
sources and sinks over large spatial scales, thereby reducing the influence of local variability and allowing fluxes to be con-
strained without detailed knowledge of all underlying environmental drivers. Previous top-down studies with two-dimensional
box models by Rhee et al. (2006) and Xiao et al. (2007) suggested that the soil sink and photochemical source were substan-
50 tially larger than found in bottom-up studies (see Table 2). Subsequent studies employing three-dimensional chemical transport
models yielded budgets more consistent with bottom-up literature, but relied on limited observational records. For example,
Pison et al. (2009) used observations from a single year (2004), Yver et al. (2011) relied on relatively few stations, mostly in
Europe, and Bousquet et al. (2011) used observations from 1991–2004, despite nearly two decades of additional observations
being available since then. Furthermore, none of these studies included observations from South America or tropical Africa,
55 regions expected to exhibit some of the largest photochemical source and soil sink fluxes globally.

In this study, we present an updated, comprehensive regional-to-global H₂ budget for 2003–2023, derived from atmospheric
H₂ inversions using the TM5 chemical transport model. We build on the work of Pieterse et al. (2013), incorporating several
updates and improvements, including updated emission inventories, a more sophisticated soil sink scheme, improved OH fields,



and higher horizontal and vertical resolution. We also exploit observations from an expanded network of H₂ monitoring sites, providing stronger constraints on regional fluxes. Finally, we evaluate our simulated H₂ mole fractions against independent observations from four aircraft campaigns.

2 Methods

The following sections describe the observations (Sect. 2.1), modelling framework (2.2), and implementation of hydrogen sources and sinks (2.3) used in this study. We then describe the setup of the forward simulations used to pre-balance global mean sources and sinks (2.4), followed by the setup of the inversion experiments (2.5).

2.1 Observations

We use H₂ mole fraction observations from multiple surface flask networks, including EUROHYDROS (EUROpean network for atmospheric HYDRogen Observations and Studies; Batenburg et al., 2011), NOAA-GML (National Oceanic and Atmospheric Administration Global Monitoring Laboratory; Pétron et al., 2024), CSIRO-GASLAB (Commonwealth Scientific and Industrial Research Organisation Global Atmospheric Sampling Laboratory; Krummel et al., 2025), MPI-BGC (Max Planck Institute for Biogeochemistry; Jordan et al., 2024), and ICOS (Integrated Carbon Observation System; Apadula et al., 2025). We also use in situ measurements from AGAGE (Advanced Global Atmospheric Gases Experiment; Prinn et al., 2025). All data are reported on the MPI-2009 calibration scale (Jordan and Steinberg, 2011). Observations span 96 monitoring sites, with some locations sampled by multiple networks (Fig. 1). Most sites do not provide continuous coverage over the full analysis period (2003–2023); details on measurement periods and sampling frequency for each network are provided in Table E1 of the Appendix. All data are filtered to retain observations representative of background conditions using available quality control and representativity flags. For NOAA-GML, only measurements analysed with a helium pulse discharge detector are used. For independent evaluation of our optimised H₂ mole fractions, we use aircraft measurements from NOAA-GML (McKain et al., 2022; Sweeney et al., 2015). These measurements include continental aircraft profiles over the United States, as well as the HIPPO (HIAPER Pole to Pole Observations; Wofsy, 2011; Wofsy et al., 2017) and ATom (Atmospheric Tomography Mission; Montzka et al., 2019; Thompson et al., 2022; Wofsy et al., 2021) campaigns, which provide pole-to-pole sampling of background atmospheric conditions across multiple altitudes. Additionally, we also use aircraft measurements from IAGOS-CARIBIC (In service Aircraft for a Global Observing System – Civil Aircraft for the Regular Investigation of the Atmosphere Based on an Instrument Container; Batenburg et al., 2016) for independent evaluation.

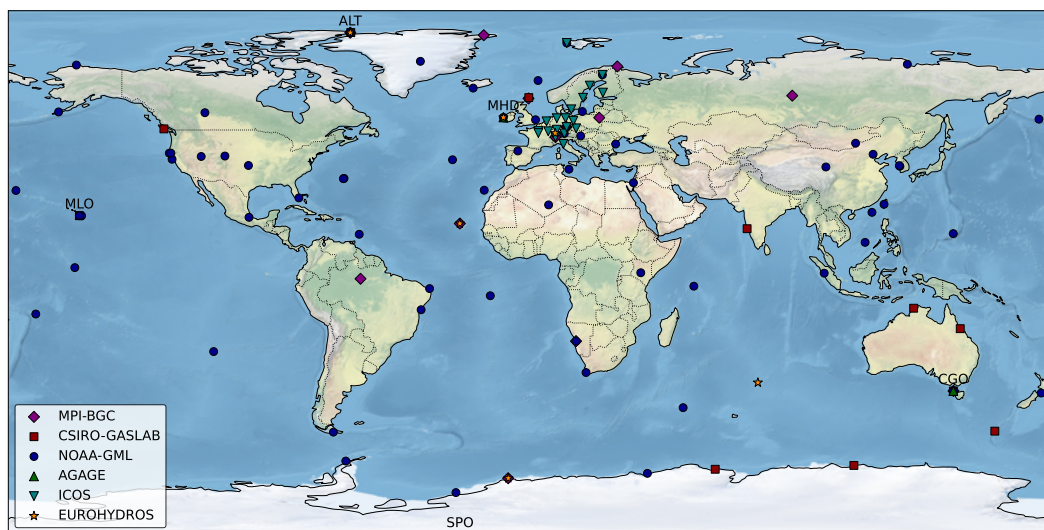


Figure 1. Global distribution of H₂ monitoring sites (N = 96) from the NOAA-GML, CSIRO-GASLAB, MPI-BGC, AGAGE, ICOS, and EUROHYDROS networks. Only sites with measurements at any time during 2003–2023 are included, with individual sites covering different sub-periods. Key sites are labelled for later reference.

85 2.2 Modelling framework

We use the TM5 three-dimensional chemical transport model (Krol et al., 2005), driven by meteorological fields from ERA5 (ECMWF ReAnalysis v5; Hersbach et al., 2020), to simulate atmospheric H₂ mole fractions. To estimate the magnitude and spatial distribution of monthly global H₂ fluxes, TM5 is coupled with the CarbonTracker data assimilation system (Van Der Laan-Luijkx et al., 2017), which employs an ensemble Kalman filter.

90 2.3 Implementation of hydrogen sources and sinks

Our modelling framework builds on Pieterse et al. (2013), with several updates and improvements. We include H₂ surface emissions as monthly fluxes at 1° × 1° resolution. Fossil fuel emissions are calculated by scaling sector-specific CO emissions from CAMS v6.2 (Copernicus Atmosphere Monitoring Service; Soulie et al., 2024) to H₂ using corresponding emission factors from CEDS (Community Emissions Data System; Hoesly et al., 2018). This approach exploits the shared origin of H₂ and CO in fossil fuel combustion and related processes such as the water–gas shift reaction, while leveraging the relatively well-constrained global CO emissions inferred from satellite observations. Oceanic H₂ emissions are spatially distributed using monthly oceanic CO fluxes (Conte et al., 2019) and scaled to 5 Tg yr⁻¹ (Price et al., 2007). This approach is based on the shared biological origin of H₂ (Walter et al., 2016) and CO (Gros et al., 2009) in the ocean, and uses CO fluxes as a proxy for biological activity. Similarly, land H₂ emissions are spatially distributed using biogenic CO land fluxes from MEGAN (Model of Emissions of Gases and Aerosols from Nature; Guenther et al., 2012) and scaled to 3 Tg yr⁻¹ (Conrad et al., 1989; Conrad,



1996; Pieterse et al., 2011). Finally, biomass burning emissions are taken from GFED5 (Global Fire Emissions Database v5; Van Der Werf et al., 2025).

We pre-calculated three-dimensional photochemical source fields from CH₂O photolysis to use in our system, by running a full-chemistry version of TM5-MP (Williams et al., 2017) with the CB05 chemical mechanism (Carbon Bond v5; Yarwood et al., 2005). The full-chemistry model included 51 species and 156 reactions, covering the oxidation chains of CH₄ and other key VOCs. Since H₂ was originally treated as a fixed species in CB05, we added H₂ production from CH₂O photolysis (Eq. 1) to the chemical scheme using the photolysis rate from Sander et al. (2006). The remaining CH₂O loss pathways were already included in CB05 (Eq. 2 and 3).



We performed the full-chemistry simulations at $3^\circ \times 2^\circ$ horizontal resolution with 34 vertical levels over 2003–2023. Chemistry was driven by the H₂ fluxes described in this section, together with CH₄ fields nudged towards surface observations and CMIP6 (Coupled Model Intercomparison Project Phase 6; Feng et al., 2020) emissions for all remaining species. We derived separate photochemical H₂ source fields for production from isoprene oxidation (hereafter the isoprene source) and from oxidation of all remaining VOCs, dominated by CH₄ oxidation (hereafter the non-isoprene source). This allows for separate specification of the flux uncertainties, with higher confidence in the non-isoprene source due to the well-characterised global abundance of CH₄. We derived the source partitioning from five sensitivity simulations in which isoprene emissions were scaled by a factor 1.0 to 0.6 (in steps of 0.1), yielding an essentially linear response in the photochemical H₂ source ($R^2 = 0.999$). We then estimated the non-isoprene source by extrapolating this relationship to zero isoprene emissions, with the isoprene source calculated as the residual relative to the base simulation (with a factor of 1.0). We have relatively high confidence in the spatial distribution of our combined photochemical H₂ source fields, based on a comparison of simulated CH₂O mole fractions with CH₂O aircraft observations from the ATom campaign, as discussed in Sect. A of the Appendix.

We calculate soil sink fluxes at $1^\circ \times 1^\circ$ resolution following scenario S3c of Pieterse et al. (2013). This approach uses the TM5 dry deposition scheme, which applies a series-resistance formulation including time-varying aerodynamic and soil resistances to compute the H₂ deposition velocity. The soil sink flux is then calculated using the deposition velocity and the near-surface H₂ mass mixing ratio in the lowest model layer at each 3-hourly time step of the simulation. In the standard configuration, the soil resistance component follows the Sanderson et al. (2003) scheme. This scheme contains formulations for seven ecosystem regions and is driven by soil moisture and soil temperature fields from ERA5 (Hersbach et al., 2020).



130 We also implemented an alternative deposition scheme in which the soil and snow resistance formulations are replaced by those of Bertagni et al. (2021). Here, the soil resistance equations include nonlinear soil moisture dynamics and depend on soil moisture, soil temperature, and porosity across eleven soil texture classes. We obtained the required soil property fields from the Global Land Data Assimilation System (GLDAS; Rodell et al. 2004). Figure 2 highlights the main differences between the two schemes. On average, the Sanderson scheme yields a 40 % larger global soil sink than the Bertagni schemes for 2003–2013. It also yields stronger uptake in subtropical regions such as northern India and South Africa, and weaker uptake in arid regions such as the Sahara and the Tibetan Plateau relative to the Bertagni scheme. Throughout the remainder of this paper, we will refer to simulations using the Sanderson and Bertagni schemes as “Sanderson” and “Bertagni”, respectively (e.g. Sanderson inversion or Bertagni inversion).

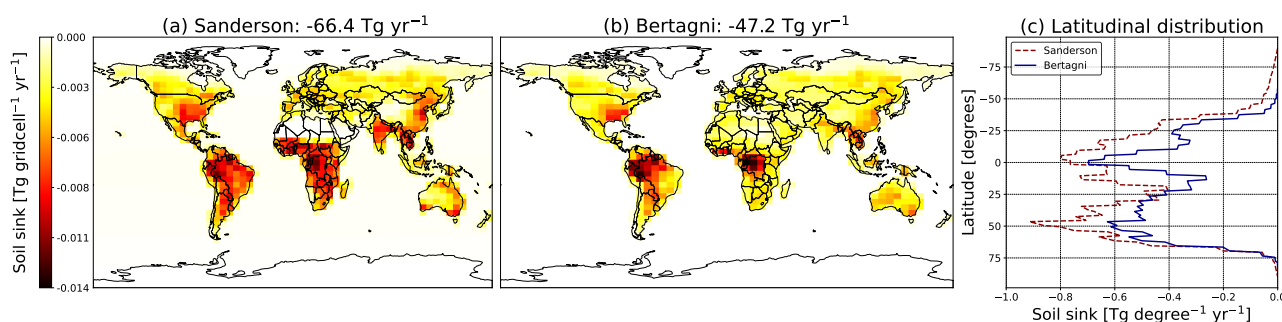


Figure 2. H₂ annual mean soil sink fluxes (2003–2013) from simulations with the Sanderson (a) and Bertagni (b) scheme. These simulations were performed using a photochemical source of 38.2 Tg yr⁻¹ (scaled by a factor of 0.7 for consistency with the literature) and no additional scaling of the soil sink (factor 1.0). Panel (c) shows the corresponding latitudinal H₂ flux distributions.

We calculate the chemical H₂ sink by oxidation with OH based on Eq. 4 using the reaction rate from Stuhl and Niki (1972). We use 3-hourly OH fields from CAMS EAC4 (Copernicus Atmosphere Monitoring Service ECMWF Atmospheric Composition Reanalysis 4; Inness et al., 2019) for the period 2003–2023 at 1° × 1° resolution with 60 vertical levels, together with the three-dimensional H₂ fields from the TM5 simulation.



In the stratosphere, we prescribe H₂ mole fractions based on the CH₄–H₂ relationship of McCarthy (2004), following Pieterse et al. (2013). This is needed since TM5 was mainly designed to simulate the troposphere and lacks advanced stratospheric chemistry and high vertical resolution. For example, important reactions such as methane oxidation by chlorine radicals and electronically excited oxygen atoms, as described by Rahn et al. (2003) and Röckmann et al. (2003), are not included in TM5. To define the troposphere–stratosphere boundary, above which the H₂ mole fractions are fixed, we use the latitude-dependent pressure threshold given in Eq. 1 of Pieterse et al. (2011). To drive the parametrisation, we use monthly CH₄ fields from CAMS EAC4 at 1° × 1° resolution, interpolated to 34 vertical levels.



2.4 Balancing global mean sources and sinks

To explore the wide range of photochemical source and soil sink estimates in the literature (Table 2), we use the TM5 model to identify source–sink configurations consistent with the observed evolution of global H₂ mole fractions. We perform forward simulations for 2003–2013 at 6° × 4° resolution with 25 vertical levels, applying uniform global scaling factors to the soil sink and combined photochemical H₂ source. We then compute four metrics using the NOAA ccgcrv curve fitting package (Thoning et al., 1989; NOAA Global Monitoring Laboratory, 2026) based on the simulated and observed H₂ mole fractions at five NOAA-GML sites (ALT, CGO, MHD, MLO, SPO): (a) detrended RMSE, (b) difference between simulated and observed mean growth rate at MLO, (c) absolute difference between simulated and observed interhemispheric gradient between ALT and SPO, and (d) absolute difference between simulated and observed seasonal amplitude at MHD. The configurations that perform best across these metrics are then used as the starting point for the subsequent Bayesian optimisation of H₂ sources and sinks.

2.5 Setup of the inversion experiments

We use the CarbonTracker Europe v3 framework (Van Der Laan-Luijkx et al., 2017) to perform a month-by-month optimisation of the soil sink and photochemical H₂ source. We run the inversion over the 2003–2023 period, with atmospheric transport simulated at 3° × 2° horizontal resolution and 34 vertical levels. We use an ensemble size of 300 members to balance performance and computational cost. We optimise the photochemical source by applying monthly regional scaling factors to the prior photochemical production fields described in Sect. 2.3. For the soil sink, we do not directly scale the fluxes as calculated within the respective schemes, as test inversions showed that this led to unstable Kalman filter performance. Instead, we optimise linearised representations of the soil sink fluxes, as explained in Sect. 2.5.1.

2.5.1 Linearisation of soil sink and stratospheric flux

The soil sink and stratospheric fixing terms were linearised in the inversions to ensure stable Kalman filter performance. This addresses a well-known limitation in Kalman-based flux optimisation arising from strongly non-linear flux-state dependencies or from initial states far from the solution, as documented in carbon cycle inversions (Tolk et al., 2011). Such conditions are applicable here, since test inversions showed that large posterior-prior adjustments in H₂ mole fractions (up to 100 ppb) were required to reconcile global mass balance, large-scale gradients, and seasonal cycles. Since both processes depend directly on the H₂ mole fraction, this introduced a non-linear coupling between fluxes and mole fractions that led to instability of the Kalman filter. Therefore, daily linearised soil sink and stratospheric fluxes were obtained from forward simulations at 3° × 2° resolution with 34 vertical levels over 2003–2023, using the Sanderson and Bertagni schemes under the best performing source-sink configurations identified in Sect. 3 in relation to four observational metrics. Our inversion results support the linearisation, as posterior mole fractions remain close to the prior (Sect. 3.2.1). Specifically, mean posterior deviations are –2.0% (Bertagni inversion) and –11.6% (Sanderson inversion), corresponding to flux differences of 1.1 and 6.6 Tg yr^{–1} under a fully first-order soil sink formulation. We deem this acceptable, as the differences are modest compared to the range of alternative prior



soil sink perturbations ($\pm 13 \text{ Tg yr}^{-1}$ relative to the base case) explored in the sensitivity analysis, which nevertheless showed convergence towards a stable posterior soil sink magnitude (Appendix Sect. C).

185 2.5.2 Spatial discretisation

We optimise the soil sink over the spatial regions used within each scheme: seven ecosystem regions for Sanderson and eleven soil texture classes for Bertagni (Table 1). In each region, the optimisation adjusts the magnitude of the linearised daily soil sink fluxes on $1^\circ \times 1^\circ$ resolution, which are effectively treated as negative surface emissions within the inversion. To introduce additional interhemispheric degrees of freedom in the state vector, the regions are subdivided at 25° N , resulting in 190 14 and 22 regions, respectively (Fig. E1). This choice accounts for the asymmetric land distribution between hemispheres and approximately balances land area between the northern and southern portions of the modelling domain. For the photochemical source, we separately optimise pre-calculated H_2 production fields from isoprene and non-isoprene oxidation, to account for differences in the uncertainties of their three-dimensional distributions. The isoprene H_2 source is optimised over the same 14 Sanderson regions as the soil sink, assuming that isoprene emissions are predominantly biogenic and ecosystem-dependent. 195 This approach reflects the short atmospheric lifetime of isoprene, which leads to relatively localised CH_2O production from its oxidation with respect to the underlying emissions. We optimise the non-isoprene H_2 source using 1° latitudinal bands, with a correlation length scale of 1000 km, yielding roughly 18 degrees of freedom from pole to pole. This reflects the relatively long atmospheric lifetime of CH_4 , the dominant precursor of CH_2O in this term, yielding a relatively uniform spatial H_2 production pattern from its oxidation.

Table 1. Summary of parameters used in the inversions, as derived in Sect. B1 and B3 of the Appendix.

	Soil sink	Isop. source	Non-isop. source
Spatial discretisation	14 ecosystems (Sanderson) 22 soil textures (Bertagni)	14 ecosystems	1° latitude bands
Correlation timescale	2 years	1 year	3 years
State-vector element uncertainty	7.5 %	5 %	2.5 %

200 2.5.3 Temporal correlation structure

To represent temporal structure in the prior flux uncertainties, we prescribe interannual correlation timescales of 3 years for the non-isoprene H_2 source, 2 years for the soil sink, and 1 year for the isoprene H_2 source. This formulation allows a component of the flux uncertainty to persist seasonally across years (e.g. January-to-January), with longer correlation times assigned to sources exhibiting weaker interannual variability (IAV) and shorter timescales to those with stronger IAV. In addition, a 3-month 205 temporal correlation is imposed across all optimised fluxes to reduce unrealistically high month-to-month flux variability and provide moderate seasonal smoothing.



2.5.4 Statevector element uncertainty

To reflect the relative confidence in our prior fluxes, we assign state vector element uncertainties across space and time of 7.5 % for the soil sink, 5 % for the isoprene H₂ source, and 2.5 % for the non-isoprene H₂ source. We note that these values can not be directly interpreted in flux space (e.g. to compute prior uncertainties in Tg yr⁻¹), as their effect on fluxes is mediated by the inversion and cannot be directly inferred.

2.5.5 Model-data mismatch

We define a model–data mismatch (MDM) of 3.0 ppb for most sites, following Pison et al. (2009). This MDM value exceeds the measurement uncertainties reported in Pétron et al. (2024), thereby allowing for additional transport and representativity errors beyond instrumental uncertainty. It is also larger than the 1 σ measurement uncertainties specified for the NOAA-GML measurements used in this study (0.78–2.82 ppb, mean 1.29 ppb). For Deep Southern Hemisphere sites, we assign a MDM of 1.5 ppb, reflecting lower transport errors (Appendix Sect. B2). When multiple observations are available on a given day for a site, the MDM for that day is scaled by the square root of the number of observations to avoid overweighting. We exclude the NOAA-GML surface flask sites AMY (Anmyeon-do, South Korea) and SDZ (Shangdianzi, China) from the optimisation, as they are strongly influenced by local fossil fuel emissions that cannot be resolved at the model’s spatial resolution. Aircraft H₂ observations are also excluded to retain them for independent evaluation.

3 Results

3.1 Balancing global mean sources and sinks

Figure 3 shows the model performance evaluated against four observational metrics, across different global scaling factors applied to the soil sink (x-axis) and photochemical H₂ source (y-axis). Here, the upper and lower panels correspond to the Sanderson and Bertagni simulations, respectively (see Sect. 2.4). Because the Bertagni scheme yields a lower prior soil sink, a broader range of scaling factors is required to span the full literature range.

We find that the source–sink balance that best agrees with global H₂ observations is close to that reported by Ouyang et al. (2025) and earlier bottom-up studies. This optimum lies in the lower-left quadrants of Fig. 3, where low RMSE (panel a), a realistic growth rate (panel b), and a realistic interhemispheric difference (panel c) are simultaneously achieved, as indicated by the green shading. In contrast, simulating a realistic seasonal amplitude (panel d) requires a substantially larger soil sink, particularly in the Sanderson simulations. This highlights the limitations of using only two global scaling factors and motivates a more elaborate inversion approach. For the Bertagni simulations, the different metrics point to a more consistent optimum, with the seasonal amplitude in better agreement with the other diagnostics. The upper-right quadrants of Fig. 3 also show that the large soil sink and photochemical source magnitudes reported by Rhee et al. (2006) and Xiao et al. (2007), derived using 2D box model inversions, perform poorly when implemented in a 3D global chemical transport model.



We identify the best-performing configurations as indicated by the black crosses in Fig. 3. Here, the global photochemical source is scaled by 0.7 and the soil sink by 0.8 (Sanderson) and 1.2 (Bertagni), corresponding to a photochemical source of 38 Tg yr⁻¹ and soil sinks of 59 Tg yr⁻¹ (Sanderson) and 54 Tg yr⁻¹ (Bertagni) in the final simulation year. These fluxes are consistent with most previous literature, including bottom-up (Ehhalt and Rohrer, 2009) and 3D inverse modelling studies (Pison et al., 2009; Yver et al., 2011; Bousquet et al., 2011). We therefore use them as the starting point for our detailed inversions (hereafter referred to as the "priors"). Additionally, we define two alternative prior configurations for the Sanderson and Bertagni scheme, with lower and higher soil sinks and photochemical sources. These alternative configurations (black triangles) are used to assess the sensitivity of the inversions to the prior magnitudes, as described in Appendix C.

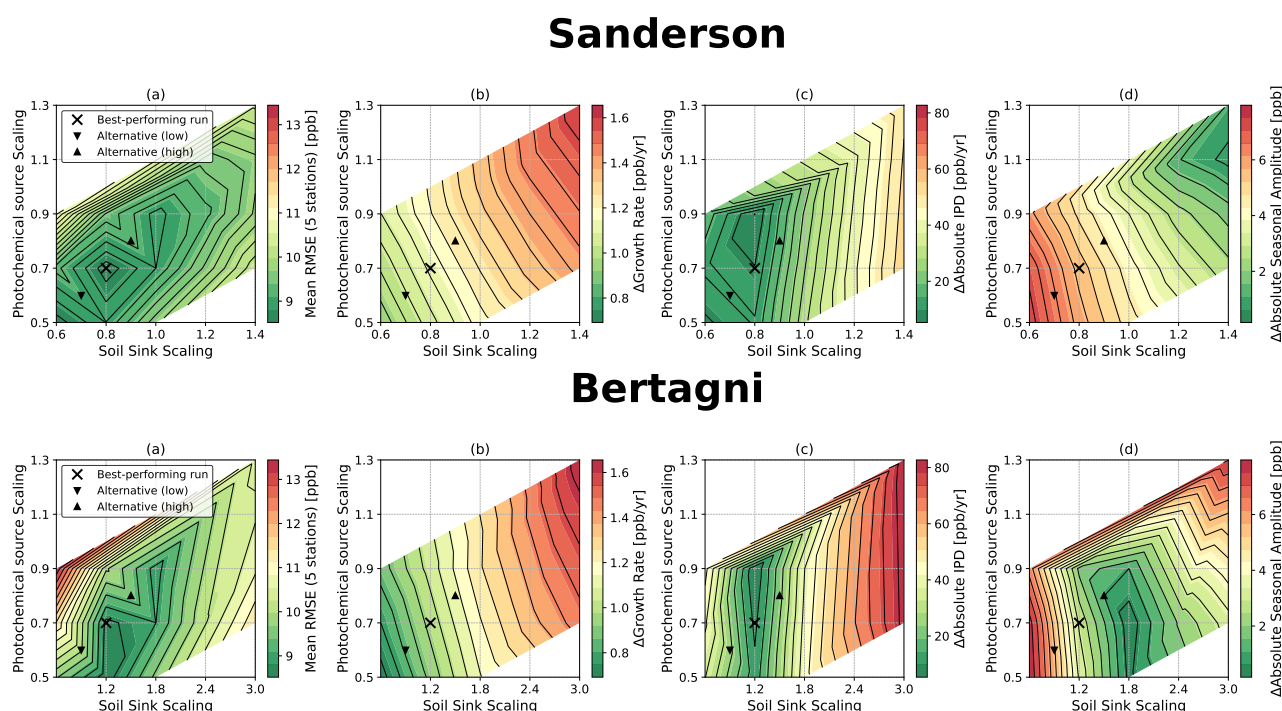


Figure 3. Sensitivity analysis for various source-sink configurations using the Sanderson (top row) and Bertagni (bottom row) schemes. Shown are: (a) mean RMSE across five stations (ALT, CGO, MHD, MLO, SPO); (b) Δ Growth Rate at MLO; (c) Δ Interpolated Difference (ALT-SPO); and (d) Δ Absolute Seasonal Amplitude at MHD.

245 3.2 Inversions

3.2.1 Evaluation with surface and aircraft observations

Due to the larger freedom to adjust sources in sinks, our detailed inversions substantially improve the agreement between simulated and observed H₂ mole fractions used in the inversions. Globally, the mean residual across all sites decreases from 69.6 (prior) to -0.8 ppb (posterior) in the Sanderson inversion, and from 11.0 (prior) to -0.7 ppb (posterior) in the Bertagni



250 inversion. Figure 4 shows that our inversions accurately capture the long-term growth rate and seasonal cycle at ALT (panel a) and SPO (panel b), representing the Northern and Southern Hemisphere, respectively. In addition, panel c shows that the inversions generally improve the fit to independent aircraft observations from the ATom, HIPPO, NOAA-GML, and IAGOS-CARIBIC campaigns, giving additional confidence in the results. A more detailed evaluation against aircraft measurements is provided in Table E2 in the Appendix, showing a modest latitudinal gradient in MAE, with generally lower values in the
255 Southern Hemisphere, while altitudinal differences are less systematic and vary between campaigns.

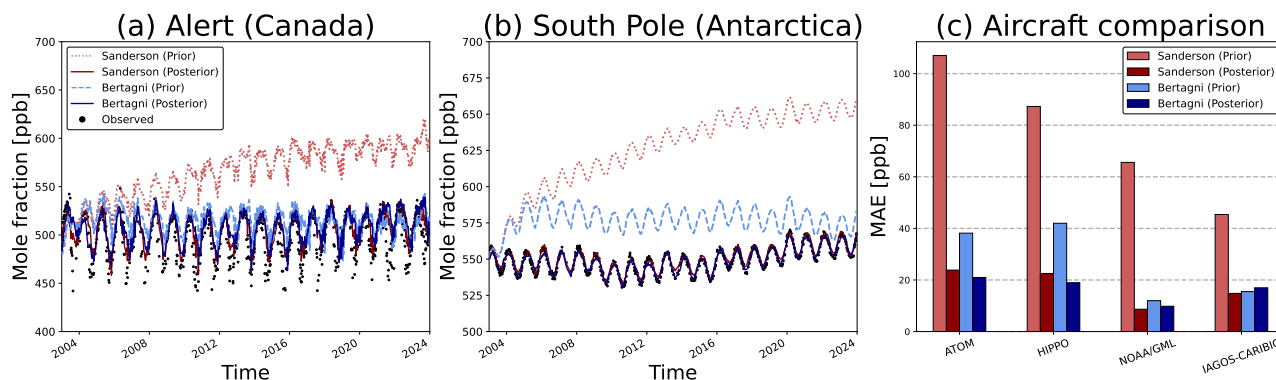


Figure 4. Time series of observed (black dots) and simulated (coloured lines) H₂ mole fractions at ALT (panel a) and SPO (panel b). Dotted and dashed lines show simulations before optimisation (prior), solid lines show simulations after optimisation (posterior). Red indicates Sanderson inversion, blue indicates Bertagni inversion. Panel (c) shows the prior and posterior mean absolute error (MAE), quantifying how well our simulated mole fractions match independent aircraft measurements from four campaigns. Here, the bars are ordered from left to right as Sanderson prior, Sanderson posterior, Bertagni prior, and Bertagni posterior for each campaign.

3.2.2 The global hydrogen budget

We find a global mean photochemical source of 34.6 Tg yr⁻¹ [29.2–38.2] and a soil sink of 52.8 Tg yr⁻¹ [47.8–56.7] for the period 2003–2023 (Table 2). Here, the central values represent the mean of our best-estimate Sanderson and Bertagni inversions (hereafter referred to as the “posterior”), and the bracketed values denote the posterior error range derived in Sect. C of the
260 Appendix. Figure 5 shows that our posterior photochemical source is lower than most previous estimates (12 of 15 studies) but remains within the one-standard-deviation range given by Ouyang et al. (2025). It also shows that our posterior soil sink agrees well with most previous studies and is close to the Ouyang et al. (2025) ensemble mean. However, our posterior error range is much narrower than their soil sink one-standard-deviation range (32–68 Tg yr⁻¹), despite covering a broad range of inversion parameters.



Table 2. Optimised global H₂ budget for 2003–2023 based on the mean of the best-estimate inversions using the Sanderson and Bertagni soil sink schemes. Posterior error ranges (bracketed values) are derived in Appendix Sect. C. Literature values are shown for comparison, noting differences in analysis periods.

	This study ^a	BU ^b	TD ^c	Ouyang et al. (2025) ^d
<i>Sources</i>				
Fossil fuel burning	14.1	14.4–20.0	15.0–22.0	7.5 [3.6–11.4]
Biomass burning	13.6	9.0–20.0	16.0	11.6 [7.9–15.3]
Land N ₂ -fixation	3.0	0.0–4.0	6.0	3.1 [0.6–5.6]
Ocean N ₂ -fixation	5.0	4.0–6.0	6.0	4.9 [1.8–8.0]
Photochemical source	34.6 [29.2–38.2]	30.2–47	38.6–76.0	38.4 [32.3–44.5]
<i>Sinks</i>				
Soil sink	52.8 [47.8–56.7]	52.9–58.5	43.5–88.0	50 [32–68]
Chemical loss	19.2 [19.1–19.7]	15.0–22.8	15.0–19.0	18.4 [16.2–20.6]

^a Includes stratospheric fixing term, with mean magnitude of 3.3 Tg yr⁻¹ (Sanderson) and 0.2 Tg yr⁻¹ (Bertagni) over 2003–2023.

^b Bottom-up studies (Novelli et al., 1999; Hauglustaine and Ehhalt, 2002; Sanderson et al., 2003; Price et al., 2007; Yashiro et al., 2011; Pieterse et al., 2011, 2013; Paulot et al., 2021; Sand et al., 2023).

^c Top-down studies using 2D (Rhee et al., 2006; Xiao et al., 2007) and 3D models (Pison et al., 2009; Bousquet et al., 2011; Yver et al., 2011).

^d Recent bottom-up study. First value denotes ensemble mean; brackets denote ±1 standard deviation.

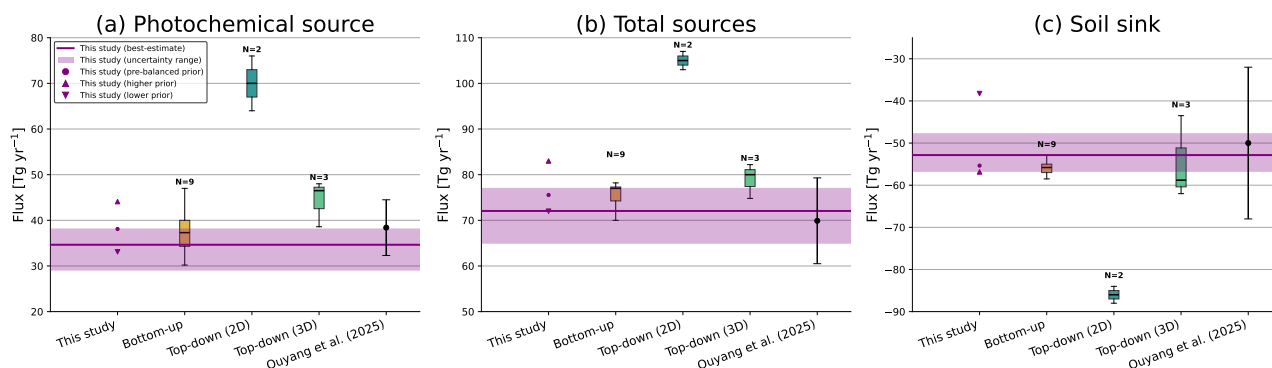


Figure 5. Comparison of our fluxes with previous studies. Purple dots and triangles indicate the mean of our pre-balanced priors and alternative priors (Sanderson and Bertagni), respectively (see Sect. 3.1). Horizontal purple lines with shading show our posterior and posterior error range as derived in the Appendix. Previous studies are summarised in box plots grouped by methodological approach (see Table 2), with N denoting the number of studies in each group and whiskers extending to 1.5 IQR. Estimates from Ouyang et al. (2025) are shown as black circles with ±1 standard deviation whiskers.



265 3.2.3 Spatial variability

We find a high degree of consistency between the posterior-prior flux corrections applied in the Sanderson and Bertagni inversions. For the soil sink, both inversions infer weaker uptake in the Northern Hemisphere mid-latitudes and stronger uptake in the tropics compared to their priors. This reflects reduced uptake in the RECCAP2 (Regional Carbon Cycle Assessment and Processes Phase 2; Ciais et al., 2022) regions of Europe, North America, East Asia, and Russia, and increased uptake in South America, Africa, and Southeast Asia (see Appendix Figs. E2, E3, E4, E5). Figure 6 shows that relative to the Ouyang et al. (2025) ensemble mean, our posterior soil sink is roughly 45% and 70% stronger in South America and Russia and 45% and 35% weaker in the Middle East and Oceania, respectively. For the non-isoprene H₂ source, both inversions yield an increase in the Northern Hemisphere (15.7 Tg yr⁻¹ Sanderson; 15.9 Tg yr⁻¹ Bertagni, up from 15.4 Tg yr⁻¹) and a decrease in the Southern Hemisphere (10.9 Tg yr⁻¹ Sanderson; 10.8 Tg yr⁻¹ Bertagni, down from 11.8 Tg yr⁻¹) relative to the prior. This corresponds to larger sources over Europe, North America, East Asia, and the Middle East, and smaller sources over South America and Oceania (Appendix Figs. E2, E3, E4, E5). For the isoprene H₂ source, both inversions infer a consistent decrease across latitudes, with the largest reductions in the Southern Hemisphere (4.7 Tg yr⁻¹ Sanderson; 5.0 Tg yr⁻¹ Bertagni, down from 7.0 Tg yr⁻¹).

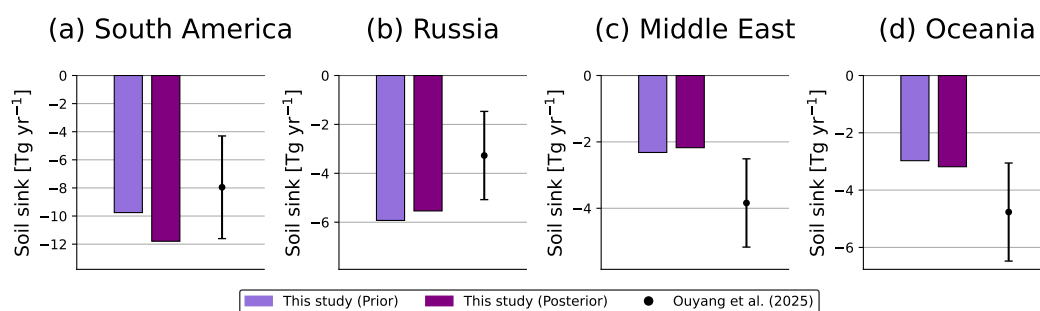


Figure 6. Photochemical source and soil sink fluxes (2003–2023 mean) for four selected RECCAP2 regions. Light bars show the prior and dark bars the posterior, taken as the mean of the Sanderson and Bertagni inversions. Black dots with whiskers show the ensemble mean and one standard deviation range from Ouyang et al. (2025).

3.2.4 Long-term growth rate of atmospheric hydrogen

Figure 7 (panels a and b) shows the observed annual H₂ growth rate over 2003–2023 (grey bars), alongside the simulated posterior growth rate (purple bars). The record exhibits three distinct stages, most clearly at SPO: a moderate growth rate from 2003–2008, a decline from 2008–2016, and a subsequent increase after 2016. Panel (c) shows that the prior biomass burning emissions (GFED5) partially explain this behaviour, with emissions decreasing after 2008. However, this is insufficient to fully reproduce the observed growth rate in the prior simulations. In the posterior, the fit to the growth rate is primarily improved by adjusting the non-isoprene H₂ source (panel d), consistent with the hypothesis of Ouyang et al. (2025) that CH₄-driven photochemical production is a dominant control on the atmospheric H₂ growth rate. Crucially, our inversions also display a



290

weakening of the global soil sink over the last two decades, a pattern absent in the priors. Specifically, the soil sink weakens on average by 0.23 Tg yr^{-2} across both inversions (Sanderson: 0.26 , Bertagni: 0.20 Tg yr^{-2}). This finding warrants further investigation given its potential implications for future atmospheric H_2 levels under the expected increase in anthropogenic emissions during the energy transition.

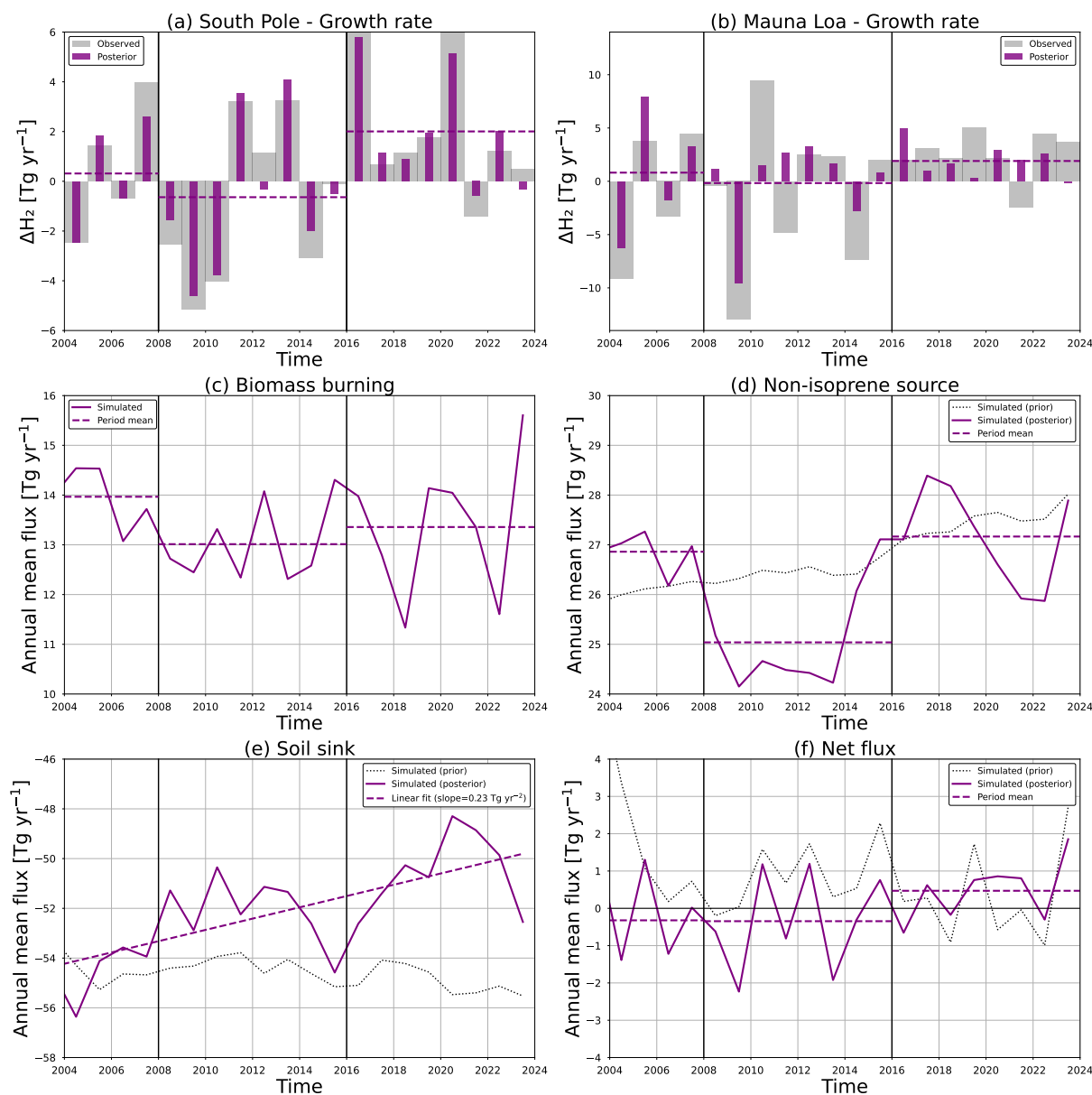


Figure 7. Observed and simulated (posterior) annual growth rates at SPO (a) and MLO (b). Panels (c–f) show global annual fluxes for (c) biomass burning, (d) non-isoprene H_2 source, (e) soil sink, and (f) net sources and sinks. The vertical lines delineate three periods (2003–2008, 2008–2016, 2016–2024) that characterise the observed H_2 growth rate.

3.2.5 Interannual variability of the soil sink

We find a clear sensitivity of the soil sink to the El Niño–Southern Oscillation (ENSO). This response is strongest in tropical South America (Fig. 8) but remains statistically significant globally, including weaker but significant correlations for several other regions (Table 3). We hypothesise that ENSO primarily influences the soil sink through soil moisture. According to Bertagni et al. (2021), most regions, including tropical South America, are dominantly diffusion-limited (i.e. too wet). Therefore, the drier conditions associated with El Niño may temporarily reduce the diffusive barrier and increase the soil sink, whereas wetter conditions during La Niña increase the diffusive barrier and dampen the soil sink. This could explain the upper right and lower left quadrants of Fig. 8, respectively. Notably, this ENSO–soil sink relationship was only very weakly present in the priors, but emerges much more clearly in the posteriors, highlighting the additional information provided by the atmospheric constraints.

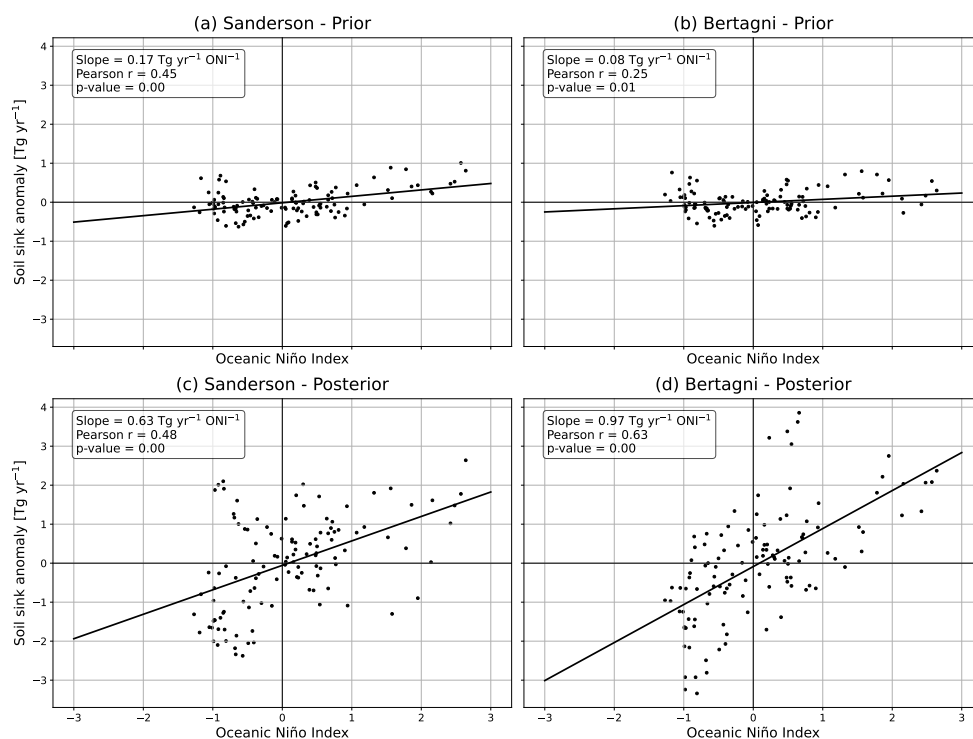


Figure 8. Monthly soil sink flux anomalies for tropical South America (RECCAP2 region), defined relative to a month-specific climatology over the final 10 years of the inversions (2014–2024), plotted against the Oceanic Niño Index (Barnston et al., 1997). Left panels correspond to the Sanderson inversion, right panels to the Bertagni inversion.



Table 3. Correlation statistics between monthly posterior soil sink anomalies and the Oceanic Niño Index (ONI). Soil sink anomalies are computed at monthly scale as deviations from a month-specific climatology over the final 10 years of the inversions (2014–2024). Metric r is the Pearson correlation coefficient, and p the p -value. Only regions showing a statistically significant relationship ($p < 0.05$) in either the Sanderson or Bertagni inversion are shown.

Region	Sanderson			Bertagni		
	Slope [$\text{Tg yr}^{-1} \text{ ONI}^{-1}$]	r	p	Slope [$\text{Tg yr}^{-1} \text{ ONI}^{-1}$]	r	p
Global	0.98	0.21	0.02	2.11	0.50	0.00
South American Tropical	0.63	0.48	0.00	0.97	0.63	0.00
Southern Africa	-0.46	-0.33	0.00	0.13	0.16	0.09
South American Temperate	0.21	0.26	0.00	0.34	0.54	0.00
Tropical Asia	0.19	0.29	0.00	0.25	0.32	0.00
Europe	0.16	0.40	0.00	0.16	0.31	0.00
North American Temperate	0.10	0.24	0.01	0.19	0.33	0.00
North American Boreal	0.09	0.18	0.05	0.14	0.31	0.00

4 Discussion and outlook

4.1 Uncertainty and potential aliasing in the inferred H_2 budget

We have high confidence in our inferred soil sink, as the only other major sink in the hydrogen budget, oxidation by OH, is relatively well constrained. We are also confident in our inferred total sources, although constraining the photochemical source is more challenging. This arises from the fact that several other sources in the hydrogen budget are prescribed in our inversions rather than optimised, introducing a potential for aliasing, whereby biases in these prescribed terms are compensated by adjustments in the posterior photochemical source or soil sink. For example, the three-stage pattern in our posterior photochemical source could also partly reflect a systematic underestimation of biomass burning H_2 emissions in the GFED5 prior, which showed a similar temporal structure. However, this is unlikely to fully explain our inferred trend, as GFED5 H_2 emissions already lie at the upper end of current literature estimates (Ouyang et al., 2025).

Similarly, sources not included in our model provide an additional pathway for aliasing. For example, geological sources and leakage-related industrial emissions were omitted due to the lack of robust emission inventories and their expected small magnitude (Ouyang et al., 2025). If sufficiently large and increasing over time, these fluxes could in principle contribute to the inferred weakening of the global soil sink. This is unlikely for geological sources, for which no clear mechanisms support a sustained long-term increase. Industrial emissions provide a more plausible pathway, as global hydrogen demand increased from 52.5 Tg in 2000 (IEA, 2019) to 95 Tg in 2023 (IEA, 2023), implying an approximate doubling of emissions under constant loss rates. However, fully explaining our inferred soil sink trend (4.8 Tg yr^{-1} reduction over 2003–2023) would require losses of approximately 11.3 % across the hydrogen supply chain. This lies at the upper end of literature estimates ($\sim 10\%$) and well



above current best estimates (1.3%) (Trapani et al., 2025), suggesting that industrial emissions may contribute but are unlikely
320 to fully explain our inferred trend.

A possible misattribution of sources and sinks of H₂ could be evaluated by propagating our H₂ fluxes into simulated hydrogen
deuteride (HD) abundances, following an approach similar to Pieterse (2013). While the photochemical source has limited
isotopic leverage, the soil sink enriches the atmosphere in HD (Chen et al., 2015). We therefore expect that a decreasing soil
sink would contribute to declining global HD levels over time. In the case of a strong increase in industrial or geological
325 emissions, we also expect declining HD levels, since these sources are heavily isotopically depleted (Gibson et al., 2024).
However, no HD observations have been published over the past 15 years, meaning this cannot be tested. In addition, other
sources and sinks with greater isotopic fractionation have likely evolved in recent decades, as well as their corresponding
source signatures. For example, the isotopic signature of fossil fuel emissions has likely changed due to advances in engine
technology (Vollmer et al., 2010); however, such changes remain poorly characterised.

330 Our inverse problem is further complicated by the opposing signs and substantial spatial overlap of the soil sink and photochemical source (particularly the isoprene-related partition), both of which peak in tropical regions, leading to strong posterior correlations between these flux components (see Appendix Sect. D). Flux separability is further complicated by the low observational density in these regions. As recently noted by Tardito Chaudhri and Stevenson (2025), local process-based measurements are crucial for improving understanding of tropical soil H₂ fluxes. We further emphasise the need for expanded
335 atmospheric mole fraction observations to constrain future inverse modelling studies, as these regions remain among the least observed globally. A challenge specific to the photochemical source is its three-dimensional nature, making it more difficult to constrain using surface observations alone (Bousquet et al., 2011). Despite this, we consider multi-species inversions a promising approach to better quantify this term, given the strong chemical coupling between H₂, CH₂O, CO, and OH. Pison et al. (2009) applied such a framework, however we identify a clear opportunity to revisit it in light of nearly two decades of satellite
340 observations of CO and CH₂O since then.

4.2 Indications of an overestimated CH₂O photolysis rate in CB05

We found a significantly lower posterior photochemical H₂ source compared to the prior derived from the full-chemistry simulation. This reduction occurred mainly in the pre-optimisation with global scaling factors (Sect. 3.1), but also in the subsequent detailed inversions (Sect. 3.2). It suggests that in our full-chemistry simulations, either CH₂O mole fractions (the
345 final precursor of H₂) were too large, or the photolysis rate of CH₂O was too large. We consider the former unlikely, as simulated CH₂O is already consistently biased low relative to aircraft observations, with a mean bias of -35.5 % across all ATom flights (see Appendix Sect. A). We consider it more likely that the photolysis rate is too large, as in the updated CBM4 (Carbon Bond v4) and subsequent CB05 mechanism, it was increased by 30 % relative to the original version of CBM4 to improve simulated CO, CH₄, and O₃ (Williams and Van Noije, 2008). However, the impact of an enhancement of the H₂-producing photolysis
350 channel on H₂ was not investigated in this study. An overestimated photolysis rate would also lead to more removal of CH₂O, consistent with our relatively low simulated CH₂O mole fractions. Finally, Pieterse et al. (2013) obtained a photochemical H₂ source consistent with both the literature and our posterior using an otherwise similar chemistry scheme, but with the



lower CBM4 photolysis rate. All in all, we recommend further investigation into the updated photolysis rate of CH₂O for the molecular channel used in CB05.

355 4.3 Implications of ENSO-driven soil uptake variability for other trace gases

Our inferred H₂ soil sink sensitivity to ENSO likely extends to other trace gases such as CH₄, CO, N₂O and COS, since their uptake efficiency also depends on gas diffusion through the soil pore network. When soils become water-saturated, diffusion is reduced as pores fill with water, limiting access to microbial or chemical sinks. Field measurements support this theory, as Aronson et al. (2019) conducted soil chamber measurements in a tropical forest in Costa Rica and showed that ENSO cycles
360 influence biogenic CH₄ fluxes through soil moisture changes, with CH₄ consumption highest during the driest phase of El Niño and reduced uptake during La Niña and wetter conditions. These results align with our findings and support an ENSO-driven modulation of the H₂ soil sink in tropical regions, with similar moisture-driven mechanisms proposed.

5 Conclusions

In this study, we performed atmospheric inversions of H₂ using the TM5 chemical transport model to derive a spatiotemporally
365 resolved budget over the period 2003–2023. Using this approach, we infer a global mean H₂ soil sink of 52.8 [47.8–56.7] Tg yr⁻¹ and a global photochemical H₂ source of 34.6 [29.2–38.2] Tg yr⁻¹ over 2003–2023. Notably, our soil sink posterior error range is substantially narrower than the one standard deviation range reported by Ouyang et al. (2025). We also infer a soil sink that is 45 % and 35 % weaker in the Middle East and Oceania and 45 % and 70 % stronger in South America and Russia, respectively, relative to Ouyang et al. (2025). Our results further suggest that variability in atmospheric H₂ growth rates
370 between 2003 and 2023 was primarily driven by changes in the non-isoprene photochemical source, consistent with the recent hypothesis of Ouyang et al. (2025) that CH₄-driven photochemical production is a dominant control on the atmospheric H₂ growth rate. Additionally, our results show a weakening of the global soil sink at a mean rate of 0.23 Tg yr⁻² over this period. We recommend further investigation into this, given the potential implications for future atmospheric H₂ levels in light of the projected increase in anthropogenic emissions during the ongoing energy transition. Finally, our results show a clear sensitivity
375 of the H₂ soil sink to the El Niño–Southern Oscillation, strongest over diffusion-limited soils in tropical South America, with increased uptake during drier El Niño conditions and reduced uptake during wetter La Niña conditions. This sensitivity may extend to other tracers, such as CH₄, CO, N₂O, and COS, given that their uptake is also dependent on diffusion through the soil pore network.

To further improve quantification of the global hydrogen budget, progress is needed along two complementary directions:
380 improved process understanding to refine prior flux estimates and expanded observational constraints for future inverse modelling studies. For process understanding, additional field measurements of the soil sink across a broad range of environments are key, with particular emphasis on tropical regions, as noted by Tardito Chaudhri and Stevenson (2025). For observational constraints, expanding H₂ mole fraction measurements in the tropics should be a priority, given the large fluxes and sparse observational coverage in these regions. Measurements and simulations of HD may provide additional constraints on the global



385 H₂ budget, as demonstrated by Pieterse et al. (2013). However, the potential of HD is limited by the absence of observations over the past 15 years, as well as limited progress in constraining source signatures and fractionation factors. Finally, for the photochemical H₂ source, we consider multi-species inversions a promising approach given the strong chemical coupling between H₂, CH₂O, CO, and OH. Pison et al. (2009) applied such a framework, and we identify a clear opportunity to revisit it in light of nearly two decades of satellite observations of CO and CH₂O since then.



390 Appendix A: Evaluation of simulated formaldehyde levels with aircraft observations

To assess whether our simulated photochemical production fields provide a reasonable starting point for the inversions, we compare our TM5 full-chemistry CH₂O mole fractions with aircraft observations from the ATom campaign (Hanisco et al., 2019; Wofsy et al., 2021). We find that our simulations successfully capture the increase of CH₂O over polluted continental regions, producing a near-surface land-ocean gradient of 1 ppb over North America (Fig. A1), as well as the vertical increase
 395 toward the surface due to precursor emissions. Across all flights (N = 35), our simulations reproduce the mean latitudinal and vertical gradients relatively well, despite a general underestimation of mole fractions (Fig. A2). Simulated and measured CH₂O mole fractions increase toward the equator, reflecting higher emissions of biogenic NMHCs, mainly isoprene, and toward the surface due to higher precursor emissions. Across all flights, the mean observed CH₂O mole fraction was 0.137 ppb, compared to 0.088 ppb in our simulations, yielding a mean bias of -0.049 ppb (-35.54 %; Table A1). Importantly, for the six flights with
 400 mean observed CH₂O mole fractions above 0.2 ppb, the mean bias decreased to -0.039 ppb (-15.75 %). Five of these flights sampled tropical ocean regions, where enhanced CH₄ oxidation in the tropics likely drives elevated CH₂O mole fractions, while the sixth sampled the continental U.S., where CH₄ oxidation was likely larger due to higher OH availability, together with larger anthropogenic VOC emissions that provide additional precursors. Our underestimation of simulated CH₂O mole fractions is likely related to an overestimation of the photolysis rate of CH₂O through the molecular channel, as explained
 405 in Sect. 4.2 of the Discussion. We attribute remaining discrepancies to errors in emission inventories, vertical mixing, and simulated OH levels. Finally, the reported measurement uncertainty (NASA ISAF ±10 %) may also explain some of our bias.

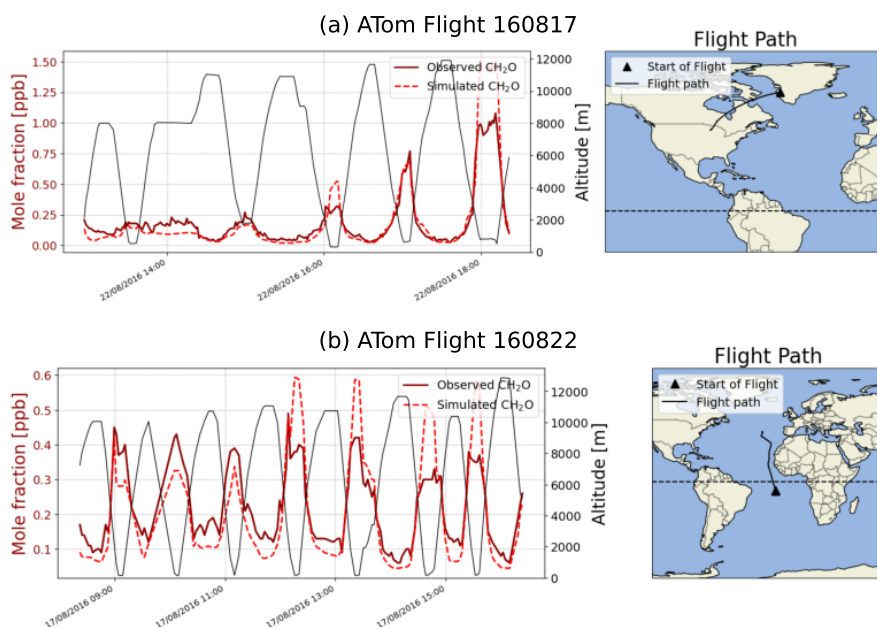


Figure A1. Observed and simulated CH₂O mole fractions for two ATom flights: (a) 160822 (mean bias: 1.5 %) and (b) 160817 (mean bias: -4.1 %). Left axis: CH₂O mole fraction; right axis: altitude along flight track.

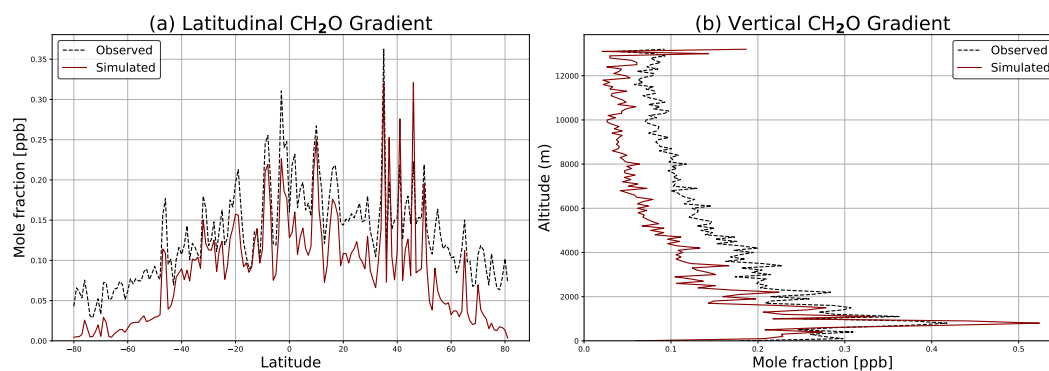


Figure A2. Latitudinal and vertical gradients in observed and simulated CH₂O mole fractions.

Table A1. Summary statistics of observed and simulated CH₂O mole fractions from ATom flights for all flights and subsets with increasing minimum observed CH₂O.

Flights	N	Mean obs. [ppb]	Mean sim. [ppb]	Mean bias [ppb]	Mean bias [%]
All	35	0.137	0.088	-0.049	-35.54
> 0.05 ppb	34	0.141	0.092	-0.049	-35.09
> 0.1 ppb	25	0.162	0.112	-0.050	-31.01
> 0.15 ppb	12	0.206	0.158	-0.048	-23.15
> 0.2 ppb	6	0.247	0.208	-0.039	-15.75
> 0.25 ppb	2	0.347	0.322	-0.026	-7.37



Appendix B: Evaluation of inversion parameters

To determine the best-performing inversion settings, we conducted various experiments at a $6^\circ \times 4^\circ$ horizontal resolution with 25 vertical levels, covering 2003–2013. We used the optimal prior Bertagni soil sink and photochemical source fluxes derived in Sect. 2.4 and the settings described in Sect. 2.5 unless stated otherwise. We use an ensemble size of 150 members, which is sufficient given our chosen uncertainties for each statevector element in space and time. However, our main results in Sect. 3.2 are still obtained with 300 members to be conservative and account for potential sensitivity to random sampling, particularly since tests showed that larger uncertainties on the statevector elements increase this sensitivity.

B1 Temporal correlations

To establish robust temporal correlations, we first examined the effect of the secondary sigma parameter in our state vector (Table B1). This parameter describes the extent to which observations from neighbouring years influence monthly scaling, and its use is based on the assumption that a large part of the error shows seasonal behaviour. In our first experiment (A1), we use a 5-year value for the non-isoprene H_2 source, assuming that CH_4 mole fractions show low interannual variability. For the soil sink, we use a 3-year value, assuming that this term is more variable, but that this variability is already partly captured in our input datasets. Finally, we use a 2-year value for the isoprene H_2 source, since its interannual variability is poorly understood and poorly constrained. Shorter timescales or uniform long timescales were also tested (Table B1).

Table B1. Impact of the secondary sigma (SS) parameter, which controls multi-year correlations, on the fraction of grid cells with optimised scaling factors that reverse the sign of the prior flux.

Experiment	SS _{soil sink} [y]	SS _{non-isoprene} [y]	SS _{isoprene} [y]	Pos _{soil} [%]	Neg _{isoprene} [%]	Neg _{non-isoprene} [%]
A1	3	5	2	3.48	2.26	6.34
A2	2	3	1	2.85	1.00	2.41
A3	5	5	5	3.56	3.05	10.98

We identify experiment A2 as the best-performing configuration, as it yields the most physically consistent and interpretable flux estimates, with the lowest fraction of grid cells in which the optimised scaling factors reverse the sign of the prior flux, resulting in positive soil sinks or negative photochemical sources (Table B1). This is illustrated for the South America REC-CAP2 region in Fig. B1, where experiments with longer temporal correlation scales (A1 and A3) show a reduced soil sink, compensated by a smaller photochemical source (panel a). This is unlikely, as it largely arises from a more negative photochemical source (panel b) and a more positive soil sink (panel c). We also find this in other regions, including Africa and Oceania (not shown here). Experiment A2 also performs better because it has a more spatially coherent optimised soil sink and a non-isoprene H_2 source, in contrast to the scattered and dipole-like patterns obtained in experiments A1 and A3. Finally, the regional fluxes of A2 show realistic interannual variability, whereas variability is strongly suppressed in A1 and A3. Based on these considerations, we adopt the secondary sigma values from experiment A2 for all remaining inversions.

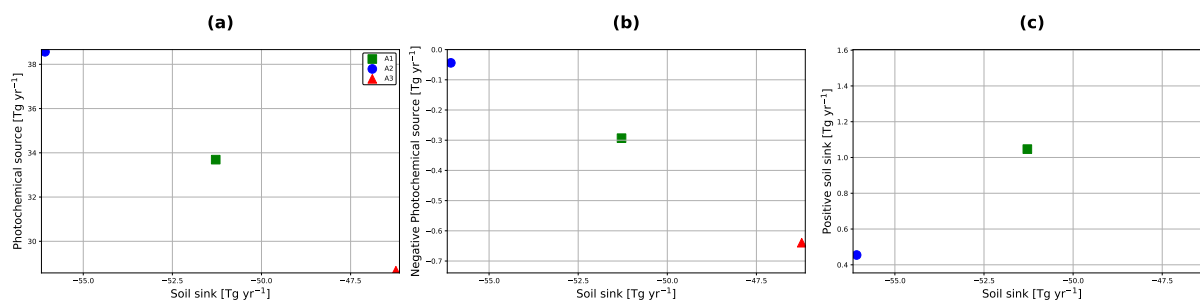


Figure B1. Annual mean H₂ fluxes over the South America RECCAP2 region (2003–2013) for the three secondary sigma experiments. Panel (a) shows the soil sink versus the photochemical source, panel (b) shows the soil sink versus the negative photochemical source, panel (c) shows the soil sink versus the positive soil sink over this region.

B2 Model-data mismatch

Next, we investigated the sensitivity of the inversions to the value of the model–data mismatch (MDM). This was achieved through offline inversions, which avoided rerunning the full transport model and reduced computational costs. In the base configuration (experiment A4), a uniform MDM of 3.0 ppb was assigned to all sites. To introduce spatially varying but physically motivated uncertainties, we performed a sequence of experiments with progressively refined site classifications. In experiment 435 A5, Deep Southern Hemisphere (Deep SH) sites were assigned a reduced MDM of 1.5 ppb to reflect their relatively low transport and representation errors (Fig. B2), while all remaining sites retained an MDM of 3.0 ppb. Experiment A6 further distinguished marine boundary layer (MBL) sites, which were assigned an intermediate MDM of 2.0 ppb in addition to the 440 reduced MDM for Deep SH sites. Finally, in experiment A7, mixed sites were assigned an MDM of 2.5 ppb, while land sites, characterised by stronger flux heterogeneity and transport uncertainty, retained the highest MDM of 3.0 ppb. We find experiment A5 performs best, because it yields a posterior chi-squared (χ^2) closest to unity at three out of four sites that we selected to represent the MDM classes (Deep SH, MBL, Mixed, and Land). Furthermore, experiment A5 produces the lowest fraction of grid cells with sign-reversing optimized scaling factors, leading to a negative non-isoprene H₂ source or a positive soil sink 445 (i.e. physically implausible fluxes), and hence we adopt its MDM classification in the remaining experiments (Table B2).

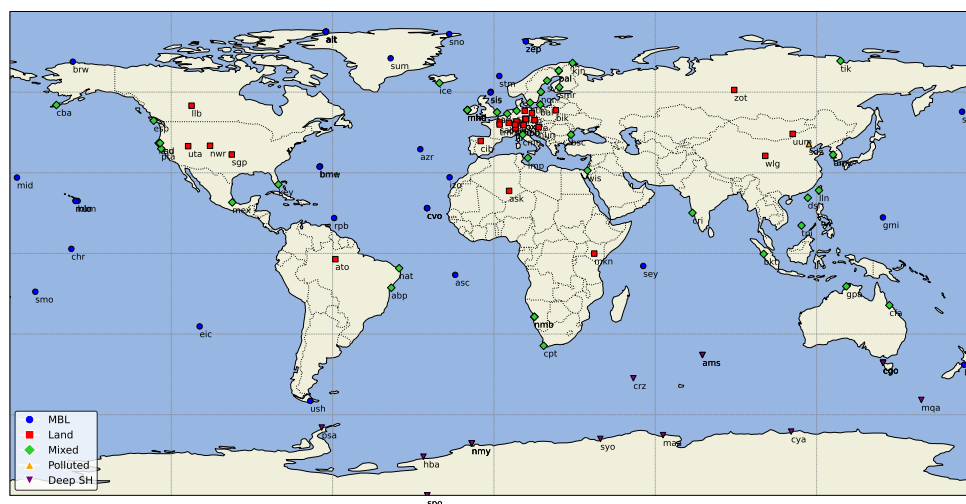


Figure B2. Global distribution of H₂ surface flask and in situ sampling sites used in this study. Sites are coloured according to their site classification: marine boundary layer (MBL), land, mixed, polluted, and deep Southern Hemisphere (Deep SH).

Table B2. Impacts of progressively refined MDM classes for different site categories on posterior chi-squared (χ^2_{post}) at MAA (Mawson, Antarctica), MLO (Mauna Loa, Hawaii), MHD (Mace Head, Ireland), and NWR (Niwt Ridge, USA). These sites represent Deep Southern Hemisphere, Marine Boundary Layer, Mixed, and Land environments, respectively. Additionally, the fraction of grid cells with optimised scaling factors that reverse the prior flux sign is shown.

	A4	A5 ^a	A6 ^b	A7 ^c
<i>Median χ^2_{post}</i>				
MAA	0.56	1.33	1.45	1.49
MLO	6.65	6.87	14.61	14.82
MHD	1.98	1.87	1.95	2.78
NWR	12.54	12.52	12.94	12.94
<i>Flux sign reversal fractions [%]</i>				
POS _{soil sink}	2.83	2.77	2.94	2.79
Neg _{isoprene}	1.07	1.19	1.29	1.29
Neg _{non-isoprene}	2.41	1.54	2.26	2.01

^a Deep Southern Hemisphere (1.5 MDM).

^b Deep Southern Hemisphere (1.5 MDM) + Marine Boundary Layer (2.0 MDM).

^c Deep Southern Hemisphere (1.5 MDM) + Marine Boundary Layer (2.0 MDM) + Mixed (2.5 MDM).

B3 Statevector element uncertainty

Lastly, we conducted offline inversion experiments by perturbing the uncertainties in our state-vector elements across space and time. This was motivated by the observed relationship between the choice of these uncertainties and the occurrence of unphysical scaling factors, which could produce either a negative photochemical source or a positive soil sink (Fig. B3), even with a 300-member inversion. We found that reducing these uncertainties improved the physical consistency of the optimised fluxes while still allowing meaningful adjustments. The initial uncertainties were 15 %, 10 %, and 5 % for the soil sink, isoprene H₂ source, and non-isoprene H₂ source, respectively. Multiplying these values by a factor of 0.5 provided an optimum balance between minimising unphysical fluxes and maintaining meaningful spatial and temporal adjustments, as shown in Fig. B3. Another reason for choosing the factor 0.5 was that lowering it further led to increasingly large posterior residuals, as denoted by panel d. Consequently, in the main inversions, uncertainties of 7.5 %, 5 %, and 2.5 % are used for the soil sink, isoprene H₂ source, and non-isoprene H₂ source, respectively.

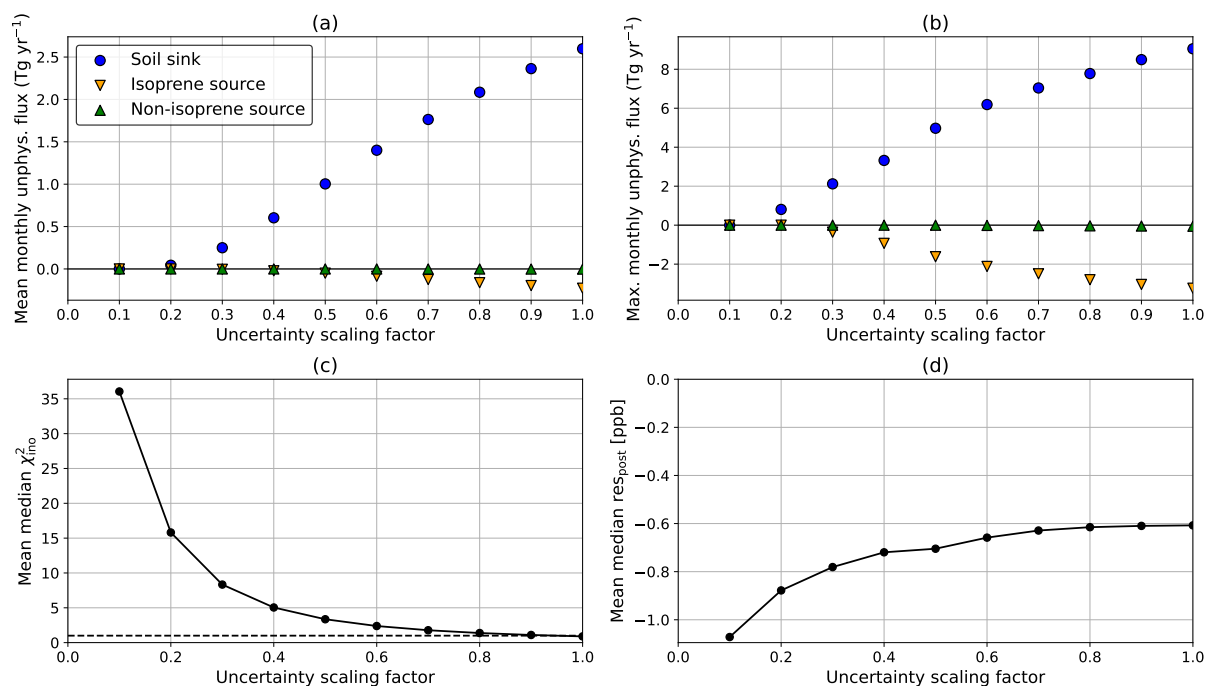


Figure B3. Sensitivity of unphysical H₂ fluxes and inversion performance metrics to the state-vector element uncertainty scaling factor (PU). (a) Monthly mean positive soil dry deposition (sink) and negative photochemical production from isoprene and non-isoprene precursors (sources). (b) Maximum monthly values of these unphysical fluxes during the runtime (2003–2023). (c) Mean of the median innovation chi-squared across all sites. (d) Mean of the median posterior residual across all sites.



Appendix C: Approximation of flux uncertainty

As shown in the previous sections, the choice of inversion parameters strongly influences the posterior fluxes inferred by the inversion. To quantify this impact, we systematically vary the number of ensemble members, observation subsets, scaling factors for the observation error variance (R), and scaling factors for the uncertainty assigned to each state vector element in space and time (P). This approach also provides a practical estimate of uncertainty within our ensemble Kalman filter-based inversion framework, for which formal posterior error estimates are otherwise not available. We perform the analysis using the best-performing configurations for the Sanderson and Bertagni schemes identified in Fig. 3.1, as well as alternative configurations shown in the same figure to assess sensitivity to the absolute magnitude of the priors. These alternative configurations correspond to prior source–sink pairs (photochemical source, soil sink) of (33.1, 36.1) and (44.1, 46.4) Tg yr⁻¹ for the Sanderson experiments, and (33.1, 40.4) and (44.1, 67.3) Tg yr⁻¹ for the Bertagni experiments. We note that scaling the prior flux magnitude also proportionally scales the assumed absolute uncertainty in flux space, thereby modifying both the prior state vector and its associated covariance matrix.

Table C1 shows that the posterior fluxes are most dependent on the absolute magnitude of the prior fluxes. In comparison, the posterior fluxes are relatively insensitive to the remaining inversion parameters. We find that the soil sink and the non-isoprene photochemical source are the most stable flux components, whereas the isoprene H₂ source shows larger variability, likely reflecting its spatial correlation with the soil sink. Apart from the absolute prior magnitudes, the largest deviations from the Base run occur in experiments with suboptimal configurations, i.e. when using a reduced number of ensemble members or a strongly limited observational network. This highlights the importance of sufficient ensemble size and observational coverage for robust flux optimisation. Even under these less constrained configurations, the inferred flux changes remain moderate, giving additional confidence to the robustness of our derived global H₂ budget. Based on all experiments in Table C1, we derive a posterior error range of 47.8–56.7 Tg yr⁻¹ for the soil sink and 29.2–38.2 Tg yr⁻¹ for the photochemical source. For the individual photochemical source components, we derive an isoprene H₂ source of 6.4–9.0 Tg yr⁻¹, and a non-isoprene H₂ source of 22.8–30.2 Tg yr⁻¹.



Table C1. Posterior H₂ fluxes from 11 offline inversions (2003–2023) in which key inversion parameters were systematically perturbed. The final two rows show posterior H₂ fluxes from two online inversions (2014–2023) using alternative source–sink configurations for the photochemical source and soil sink. All fluxes are in Tg yr^{−1}. Experiment definitions: Base denotes the ‘best-performing’ inversions used to derive our main results; P01/P10 denote scaling factors for the prior state-vector uncertainty P (0.1×, 1.0×); R05/R20 denote scaling factors for the observational error variance R (0.5×, 2.0×); NMEM75/150/225 denote the number of ensemble members; NOBS10/25/50 denote reduced observation subsets (10%, 25%, 50%); PRLOW/PRHIGH denote alternative (lower or higher) prior magnitudes.

	Soil sink		Isoprene source		Non-isoprene source	
	Bertagni	Sanderson	Bertagni	Sanderson	Bertagni	Sanderson
Base	51.8	53.9	8.2	7.7	26.7	26.6
P01	51.7	54.5	8.3	8.3	26.8	26.7
P10	51.6	53.5	8.1	7.5	26.7	26.6
R05	51.7	53.7	8.1	7.6	26.7	26.6
R20	51.8	54.1	8.2	7.9	26.7	26.6
NMEM75	51.2	55.3	8.4	8.5	26.3	27.4
NMEM150	52.0	55.9	8.7	8.4	26.4	27.7
NMEM225	52.1	54.1	8.2	7.5	26.7	27.0
NOBS10	51.5	54.5	8.1	8.2	26.7	26.6
NOBS25	51.5	54.4	8.1	8.2	26.6	26.5
NOBS50	51.5	54.4	8.2	8.1	26.3	26.7
PRLOW	48.8	47.8	6.4	6.6	22.8	22.7
PRHIGH	56.7	55.5	8.0	9.0	30.2	28.0



480 Appendix D: Spatiotemporal correlations

We find that both inversions show a strongly negative global correlation between the posterior soil sink and isoprene H₂ source fluxes (Fig. D1). This shows that regions with stronger soil uptake (more negative flux values) tend to coincide with regions of higher isoprene H₂ emissions (more positive flux values), reflecting spatial co-location of strong flux magnitudes with opposite sign conventions, particularly in the tropics. Both inversions also show a negative correlation between the soil sink and the non-isoprene H₂ source. This similarly reflects that regions of enhanced soil uptake tend to coincide with regions of enhanced emissions from this source category, despite limited spatial overlap in their dominant source regions. In contrast, the two H₂ source terms (isoprene and non-isoprene) show a positive correlation, indicating that regions with stronger emissions in one source category tend to also exhibit stronger emissions in the other. This suggests a shared spatial structure in the distribution of H₂ sources across regions.

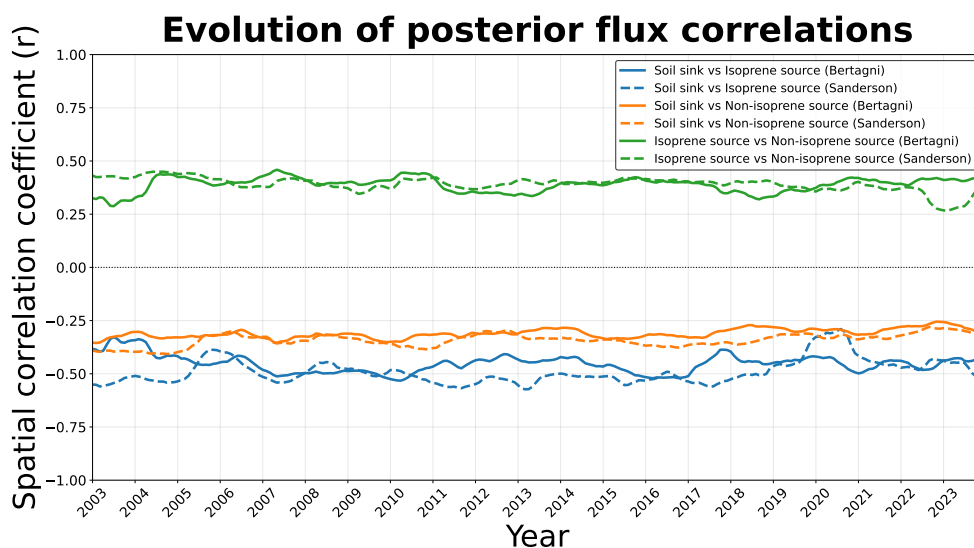


Figure D1. Temporal evolution of area-weighted spatial correlations between posterior ensemble-mean H₂ flux field. Each panel shows the Pearson correlation computed across grid cells for a given month, using cosine-latitude weighting to account for grid-cell area. Correlations are calculated from posterior ensemble-mean flux fields rather than individual ensemble members, because the ensemble Kalman filter inversion substantially reduces posterior spread, leaving residual ensemble-member variability at the grid scale comparatively small.



490 Appendix E: Additional figures and tables

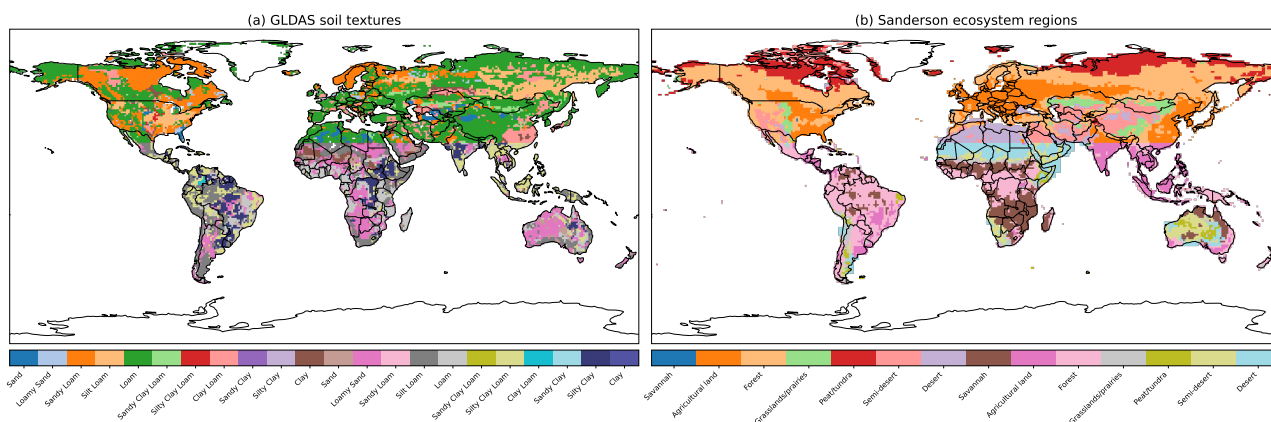


Figure E1. Regions used in the soil sink schemes and inversions (state vector regions). The left panel shows the 22 GLDAS soil texture classes, while the right panel shows the 14 Sanderson ecosystem regions. Both are split at 25° N to approximately balance the land area between the Northern and Southern portion of the domain.

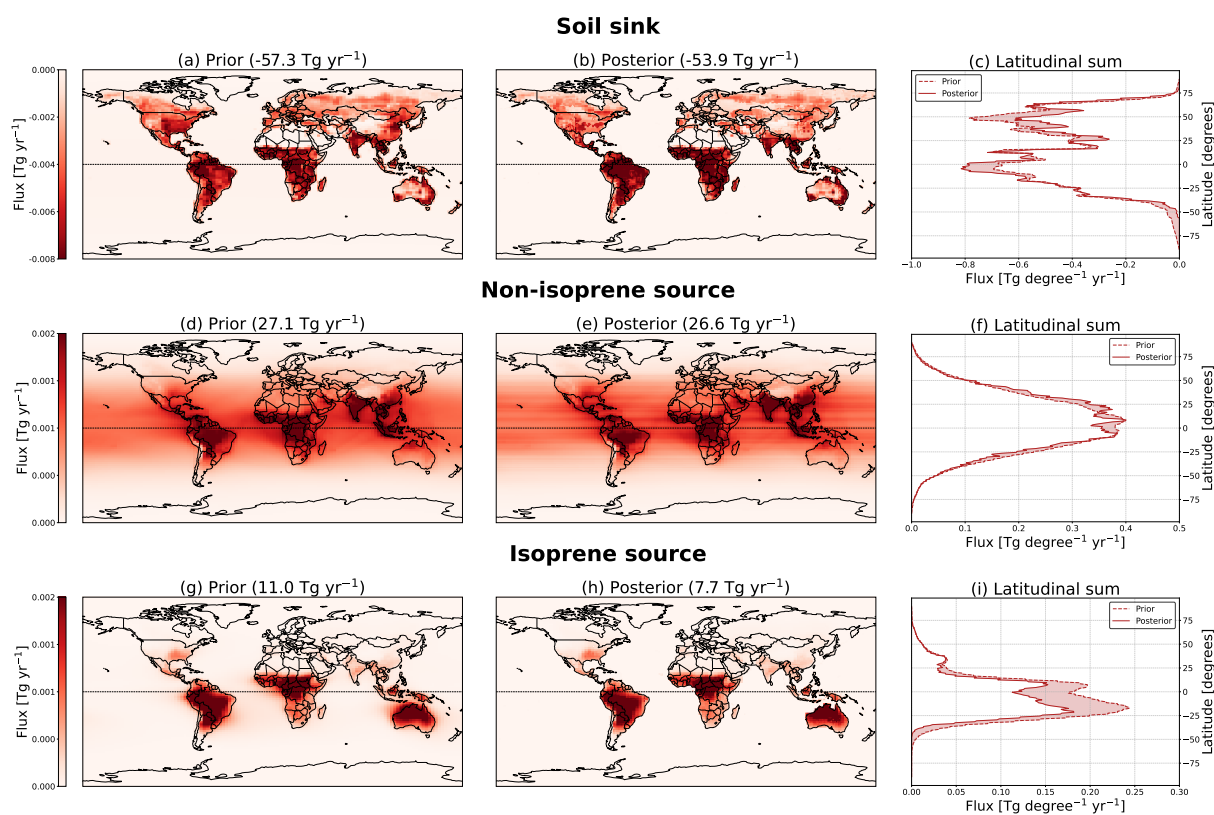


Figure E2. Global mean fluxes (2003–2023) for the Sanderson inversion, with corresponding latitudinal distributions.

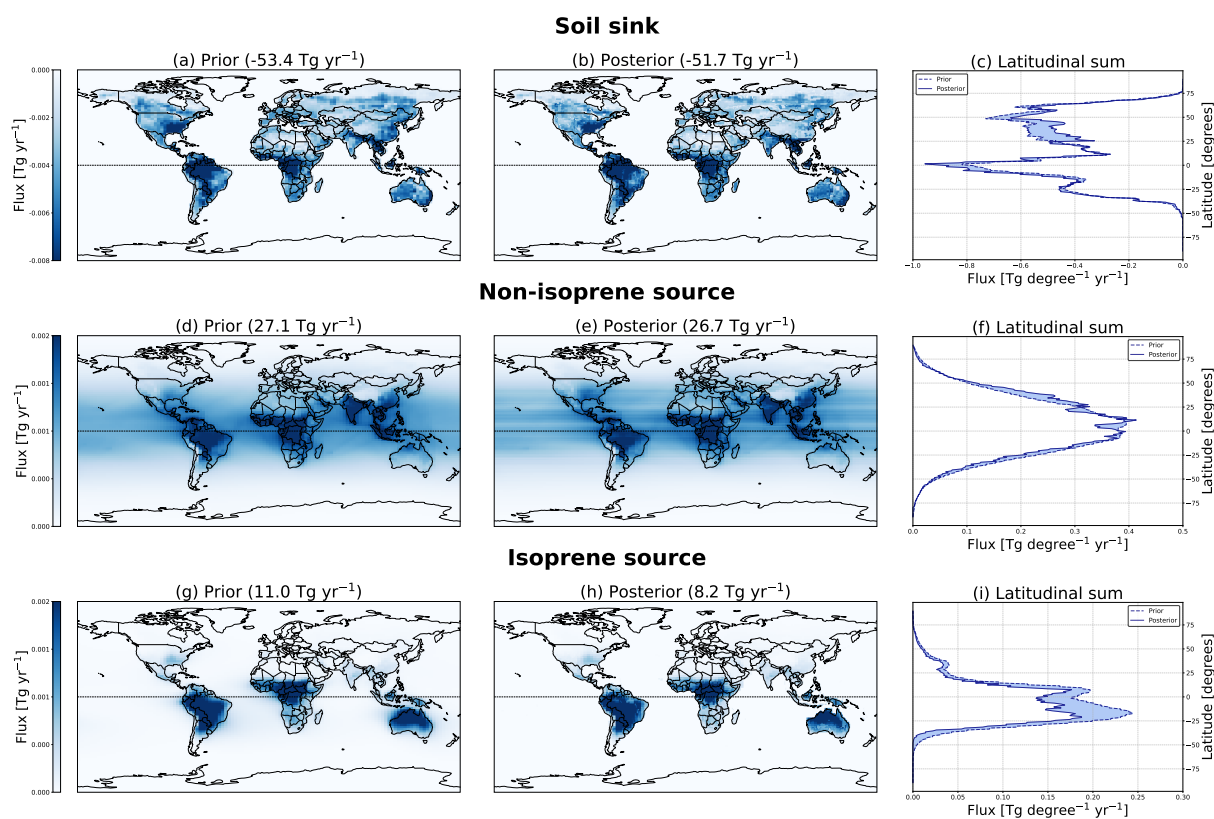


Figure E3. Global mean fluxes (2003–2023) for the Bertagni inversion, with corresponding latitudinal distributions.

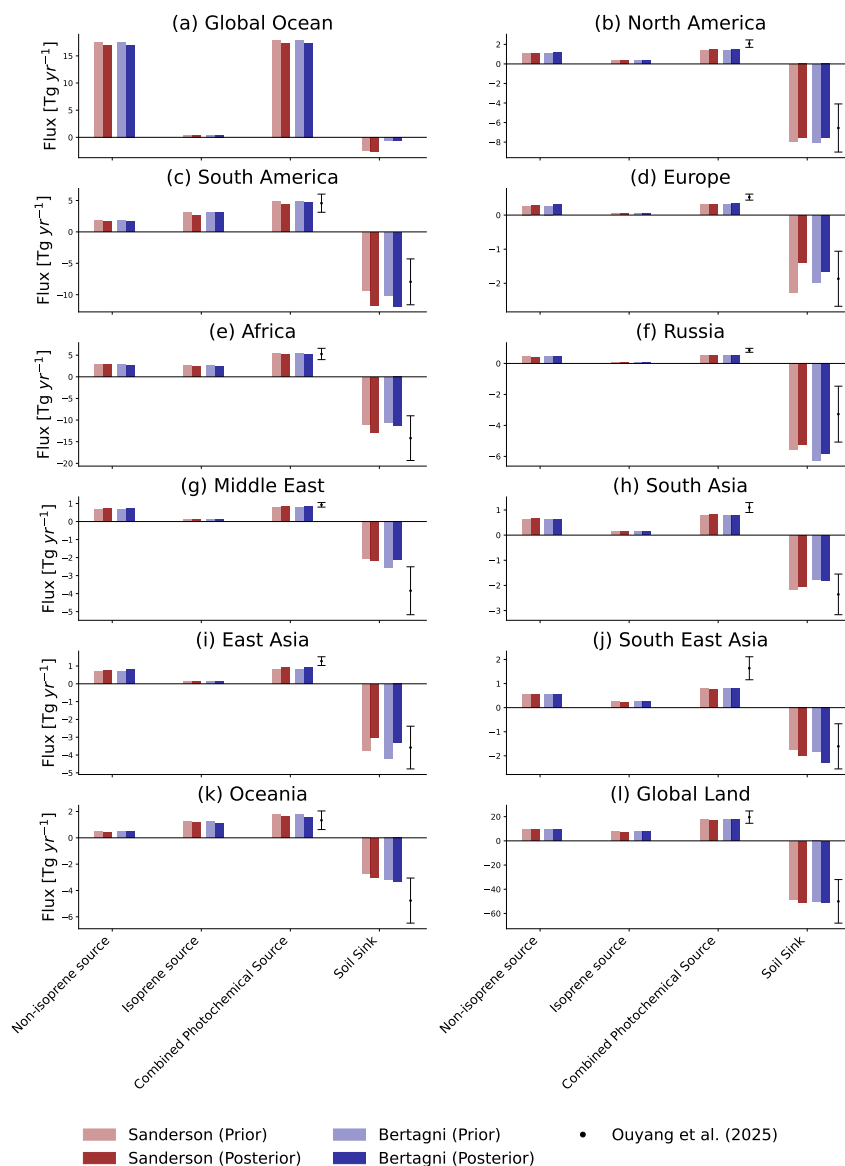


Figure E4. Fluxes per RECCAP2 region (2003–2023 mean), ordered from left to right as: Sanderson prior, Sanderson posterior, Bertagni prior, and Bertagni posterior. Black dots with whiskers show the ensemble mean and one standard deviation range from Ouyang et al. (2025). A small soil sink occurs over global ocean regions in our results (Sanderson: 2.7 Tg yr^{-1} ; Bertagni: 0.6 Tg yr^{-1}), as some islands are included in the RECCAP2 ocean regions.

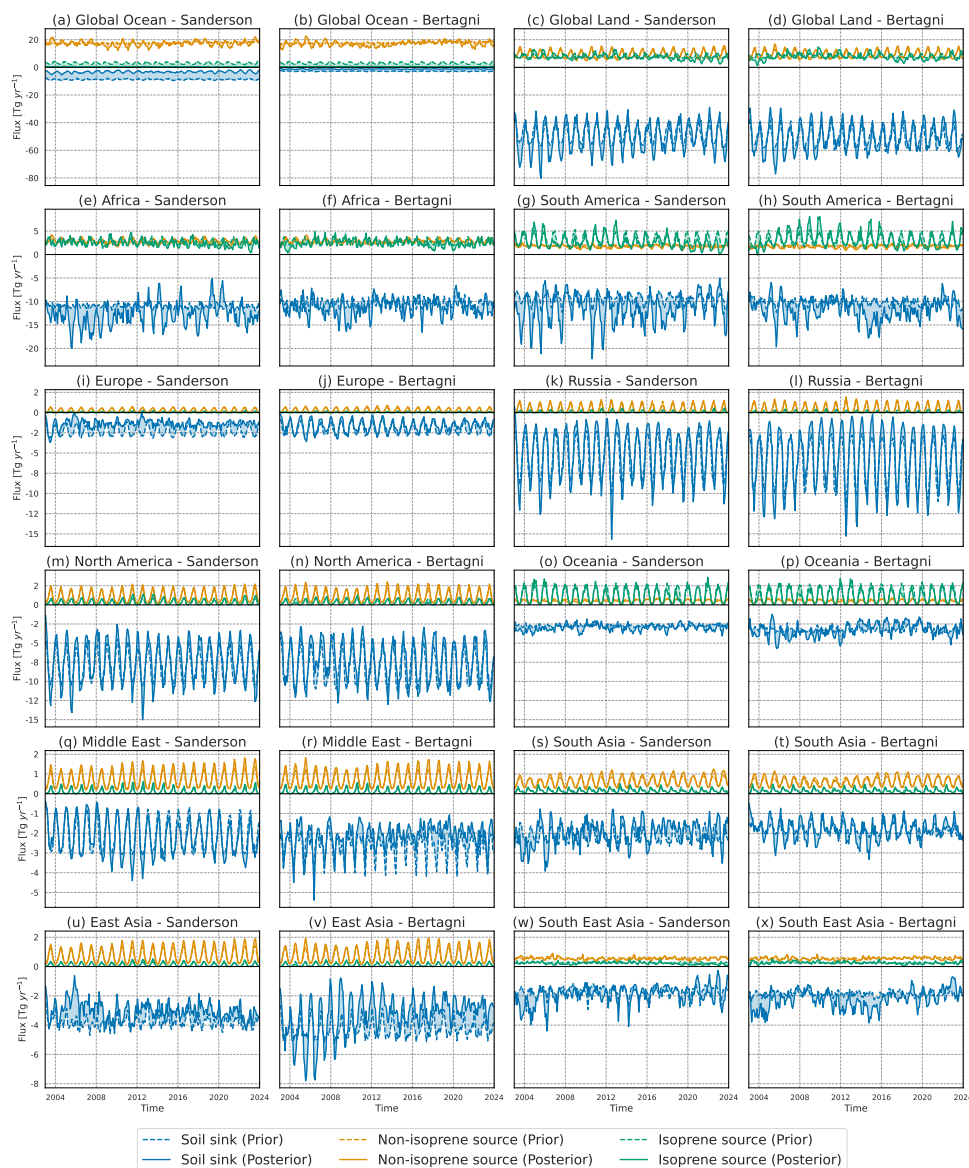


Figure E5. Monthly simulated fluxes for each RECCAP2 region in the Sanderson and Bertagni inversions. Prior fluxes are shown as dotted lines and posterior fluxes as solid lines. A small soil sink occurs over global ocean regions in our results (Sanderson: 2.7 Tg yr^{-1} ; Bertagni: 0.6 Tg yr^{-1}), as some islands are included in the RECCAP2 ocean regions.



Table E1. Overview of measurement networks used in this study, filtered for our study period (2003–2023). Sampling interval denotes the modal (i.e. most frequently occurring) time between consecutive measurements, computed across all stations or flight tracks within each network.

Network	Stations/Flights	Start date	End date	Sampling interval
<i>Surface observations</i>				
NOAA-GML	66	2007–12–13	2023–12–31	7 days
ICOS	18	2019–06–26	2023–12–31	3 days
MPI-BGC	13	2003–03–13	2023–12–20	7 days
CSIRO	11	2003–01–02	2023–12–20	7 days
EUROHYDROS	6	2005–02–09	2009–10–15	7 days
AGAGE	2	2003–01–04	2023–06–30	40 min
<i>Aircraft observations</i>				
ATom	48	2016–07–29	2018–05–21	2 min
IAGOS-CARIBIC	36	2007–05–22	2010–09–23	40 min
HIPPO	16	2009–01–09	2011–09–09	2 min
NOAA-GML	25	2009–09–28	2021–12–30	3 min



Table E2. Evaluation of posterior H₂ mole fractions against independent aircraft data. Shown are the mean posterior MAE [ppb] binned by altitude and latitude for the Sanderson (left) and Bertagni (right) inversions for each measurement campaign.

	Sanderson			Bertagni		
	90S-30S	30S-30N	30N-90N	90S-30S	30S-30N	30N-90N
<i>Below 5000 m</i>						
ATom	30.15	24.43	26.68	28.04	25.10	25.82
IAGOS-CARIBIC	–	–	–	–	–	–
HIPPO	25.23	20.11	19.67	23.46	19.22	20.13
NOAA-GML	3.00	5.77	8.98	2.36	5.64	10.25
<i>Above 5000 m</i>						
ATom	23.73	22.24	22.06	17.79	22.21	16.97
IAGOS-CARIBIC	3.04	15.70	14.44	7.93	15.99	17.45
HIPPO	26.96	23.21	22.27	20.44	21.90	14.81
NOAA-GML	3.88	6.08	9.35	8.20	5.88	10.65



Code and data availability. The CarbonTracker and TM5-MP living codebases are openly available via CarbonTracker and TM5-MP, respectively. The two-dimensional prior and posterior monthly H₂ fluxes produced in this study are archived on Zenodo at 1×1 resolution. Daily three-dimensional flux fields are available upon request.

495 *Author contributions.* FS performed the simulations, analysed and synthesised the data, produced the figures, and led the writing of the manuscript. WP supervised the study and contributed to the conceptualisation and design of the project, manuscript structure, and writing. JH contributed to the development of the model code and the design of the simulations. MK contributed to the conceptualisation and design of the project. WP, JH, and MK reviewed the manuscript.

Competing interests. The contact author has declared that neither of the authors has any competing interests.

500 *Acknowledgements.* We contacted the PIs of all observational datasets used in this study and gratefully acknowledge the EUROHYDROS (Batenburg et al., 2011), NOAA-GML (Pétron et al., 2024), CSIRO-GASLAB (Krummel et al., 2025), MPI-BGC (Jordan et al., 2024), and ICOS (Apadula et al., 2025) networks for surface flask H₂ observations, as well as the AGAGE network (Prinn et al., 2025) for in situ H₂ observations. We also acknowledge the HIPPO (Wofsy, 2011; Wofsy et al., 2017), ATom (Montzka et al., 2019; Thompson et al., 2022; Wofsy et al., 2021), NOAA-GML (McKain et al., 2022; Sweeney et al., 2015), and IAGOS-CARIBIC (Batenburg et al., 2016) campaigns for aircraft H₂ observations. ATom additionally provided CH₂O aircraft observations (Hanisco et al., 2019; Wofsy et al., 2021). AI tools (ChatGPT and 505 GitHub Copilot) were used to assist with language editing, manuscript readability, brainstorming, and coding support for analysis scripts. No generative AI tools were used to generate scientific interpretations or conclusions. All outputs were reviewed and validated by the contact author. All simulations were performed on the HPC cluster Aether at the University of Bremen, financed by DFG within the scope of the Excellence Initiative. This study also received financial support from the Nationaal Programma Groningen and the European Union via the subsidy 'Waterstof Werk: Train and Learn Hub' and by the Gas & Hydrogen Partnerships Shell Nederland.



510 References

- Apadula, F., Arnold, S., Bergamaschi, P., Biermann, T., Chen, H., Colomb, A., Conil, S., Couret, C., Cristofanelli, P., De Mazière, M., Delmotte, M., Di Iorio, T., Emmenegger, L., Forster, G., Frumau, A., Harris, E., Haszpra, L., Hatakka, J., Heliasz, M., Heltai, D., Hensen, A., Hermansen, O., Hoheisel, A., Kneuer, T., Komínková, K., Kubistin, D., Larmanou, E., Laurent, O., Laurila, T., Lehner, I., Lehtinen, K., Leskinen, A., Leuenberger, M., Levula, J., Lindauer, M., Lopez, M., Lund Myhre, C., Lunder, C., Mammarella, I., Manca, G., Manning, A., Marek, M. V., Marklund, P., Meinhardt, F., Miettinen, P., Molnár, M., Montaguti, S., Mölder, M., Müller-Williams, J., O'Doherty, S., Ottosson-Löfvenius, M., Piacentino, S., Pichon, J.-M., Pitt, J., Platt, S. M., Plaß-Dülmer, C., Ramonet, M., Rivas-Soriano, P., Roulet, Y.-A., Scheeren, B., Schmidt, M., Schumacher, M., Sferlazzo, D., Sha, M. K., Smith, P., Stanley, K., Steinbacher, M., Sørensen, L. L., Trisolino, P., Vítková, G., Ylisirniö, A., Yver-Kwok, C., Zazzeri, G., Zwerschke, E., di Sarra, A., ICOS ATC-Laboratoires des Sciences du Climat et de L'Environnement (LSCE), France, ICOS Central Radiocarbon Laboratory (CRL), Germany, ICOS Flask And Calibration Laboratory (FCL), Germany, ICOS-CAL-CRL, and ICOS-CAL-FCL: ICOS Atmosphere Release 2025-1 of Level 2 Greenhouse Gas Mole Fractions of CO₂, CH₄, N₂O, CO, meteorology and 14CO₂, and flask samples analysed for CO₂, CH₄, N₂O, CO, H₂, SF₆, delta 13C CO₂, delta 18OCO₂, delta O₂N₂ and 14C, <https://doi.org/10.18160/PP29-9CNZ>, medium: ICOS ATC time series, ICOS ATC Flask time series Version Number: 1.0, 2025.
- 515
- Aronson, E. L., Dierick, D., Botthoff, J. K., Oberbauer, S., Zelikova, T. J., Harmon, T. C., Rundel, P., Johnson, R. F., Swanson, A. C., Pinto-Tomás, A. A., Artavia-León, A., Matarrita-Carranza, B., and Allen, M. F.: ENSO-Influenced Drought Drives Methane Flux Dynamics in a Tropical Wet Forest Soil, *Journal of Geophysical Research: Biogeosciences*, 124, 2267–2276, <https://doi.org/10.1029/2018JG004832>, 2019.
- 520
- Barnston, A. G., Chelliah, M., and Goldenberg, S. B.: Documentation of a highly ENSO-related sst region in the equatorial pacific: Research note, *Atmosphere-Ocean*, 35, 367–383, <https://doi.org/10.1080/07055900.1997.9649597>, 1997.
- 530
- Batenburg, A., Walter, S., Pieterse, G., Levin, I., Schmidt, M., Jordan, A., Hammer, S., Yver, C., and Röckmann, T.: Temporal and spatial variability of the stable isotopic composition of atmospheric molecular hydrogen: observations at six EUROHYDROS stations, *Atmospheric Chemistry and Physics*, 11, 6985–6999, <https://doi.org/10.5194/acp-11-6985-2011>, 2011.
- Batenburg, A., Schuck, T., Baker, A., Zahn, A., Brenninkmeijer, C., and Roeckmann, T.: H₂ mixing ratio and isotope data from CARIBIC project, <https://doi.org/10.6084/M9.FIGSHARE.2068992.V1>, artwork Size: 809195 Bytes Pages: 809195 Bytes, 2016.
- 535
- Bertagni, M. B., Paulot, F., and Porporato, A.: Moisture Fluctuations Modulate Abiotic and Biotic Limitations of H₂ Soil Uptake, *Global Biogeochemical Cycles*, 35, <https://doi.org/10.1029/2021GB006987>, 2021.
- Bousquet, P., Yver, C., Pison, I., Li, Y. S., Fortems, A., Hauglustaine, D., Szopa, S., Rayner, P. J., Novelli, P., Langenfelds, R., Steele, P., Ramonet, M., Schmidt, M., Foster, P., Morfopoulos, C., and Ciais, P.: A three-dimensional synthesis inversion of the molecular hydrogen cycle: Sources and sinks budget and implications for the soil uptake, *Journal of Geophysical Research*, 116, D01 302, <https://doi.org/10.1029/2010JD014599>, 2011.
- 540
- Chen, Q., Popa, M. E., Batenburg, A. M., and Röckmann, T.: Isotopic signatures of production and uptake of H₂ by soil, *Atmospheric Chemistry and Physics*, 15, 13 003–13 021, <https://doi.org/10.5194/acp-15-13003-2015>, 2015.
- Ciais, P., Bastos, A., Chevallier, F., Lauerwald, R., Poulter, B., Canadell, J. G., Hugelius, G., Jackson, R. B., Jain, A., Jones, M., Kondo, M., Luijkx, I. T., Patra, P. K., Peters, W., Pongratz, J., Petrescu, A. M. R., Piao, S., Qiu, C., Von Randow, C., Regnier, P., Saunois, M., Scholes, R., Shvidenko, A., Tian, H., Yang, H., Wang, X., and Zheng, B.: Definitions and methods to estimate regional land carbon fluxes
- 545



- for the second phase of the REgional Carbon Cycle Assessment and Processes Project (RECCAP-2), *Geoscientific Model Development*, 15, 1289–1316, <https://doi.org/10.5194/gmd-15-1289-2022>, 2022.
- Conrad, R.: Soil microorganisms as controllers of atmospheric trace gases (H₂, CO, CH₄, OCS, N₂O, and NO), *Microbiological Reviews*, 60, 609–640, <https://doi.org/10.1128/mr.60.4.609-640.1996>, 1996.
- 550 Conrad, R., Mayer, H.-P., and Wäst, M.: Temporal change of gas metabolism by hydrogen-syntrophic methanogenic bacterial associations in anoxic paddy soil, *FEMS Microbiology Letters*, 62, 265–273, <https://doi.org/10.1111/j.1574-6968.1989.tb03701.x>, 1989.
- Conte, L., Szopa, S., Séférian, R., and Bopp, L.: The oceanic cycle of carbon monoxide and its emissions to the atmosphere, *Biogeosciences*, 16, 881–902, <https://doi.org/10.5194/bg-16-881-2019>, 2019.
- Cowan, N., Roberts, T., Hanlon, M., Bezanger, A., Toteva, G., Tweedie, A., Yeung, K., Deshpande, A., Levy, P., Skiba, U., Nemitz, E., and
555 Drewer, J.: Quantifying the soil sink of atmospheric hydrogen: a full year of field measurements from grassland and forest soils in the UK, *Biogeosciences*, 22, 3449–3461, <https://doi.org/10.5194/bg-22-3449-2025>, 2025.
- De Kleijne, K., Huijbregts, M. A. J., Knobloch, F., Van Zelm, R., Hilbers, J. P., De Coninck, H., and Hanssen, S. V.: Worldwide greenhouse gas emissions of green hydrogen production and transport, *Nature Energy*, <https://doi.org/10.1038/s41560-024-01563-1>, 2024.
- Ehhalt, D. H. and Rohrer, F.: The tropospheric cycle of H₂: a critical review, *Tellus B: Chemical and Physical Meteorology*, 61, 500–535,
560 <https://doi.org/10.1111/j.1600-0889.2009.00416.x>, 2009.
- Feng, L., Smith, S. J., Braun, C., Crippa, M., Gidden, M. J., Hoesly, R., Klimont, Z., Van Marle, M., Van Den Berg, M., and Van Der Werf, G. R.: The generation of gridded emissions data for CMIP6, *Geoscientific Model Development*, 13, 461–482, <https://doi.org/10.5194/gmd-13-461-2020>, 2020.
- Gibson, J., Eby, P., and Jaggi, A.: Natural isotope fingerprinting of produced hydrogen and its potential applications to the hydrogen economy,
565 *International Journal of Hydrogen Energy*, 66, 468–478, <https://doi.org/10.1016/j.ijhydene.2024.04.077>, 2024.
- Gros, V., Peeken, I., Bluhm, K., Zöllner, E., Sarda-Estève, R., and Bonsang, B.: Carbon monoxide emissions by phytoplankton: evidence from laboratory experiments, *Environmental Chemistry*, 6, 369, <https://doi.org/10.1071/EN09020>, 2009.
- Guenther, A. B., Jiang, X., Heald, C. L., Sakulyanontvittaya, T., Duhl, T., Emmons, L. K., and Wang, X.: The Model of Emissions of Gases and Aerosols from Nature version 2.1 (MEGAN2.1): an extended and updated framework for modeling biogenic emissions, *Geoscientific
570 Model Development*, 5, 1471–1492, <https://doi.org/10.5194/gmd-5-1471-2012>, 2012.
- Hanisco, T., Hannun, R., St.Clair, J., and Wolfe, G.: Atmospheric Tomography Mission (ATom)ATom: L2 Measurements of In Situ Airborne Formaldehyde (ISAF), <https://doi.org/10.3334/ORNLDAAC/1730>, 2019.
- Hauglustaine, D. A. and Ehhalt, D. H.: A three-dimensional model of molecular hydrogen in the troposphere: TROPOSPHERIC MOLECULAR HYDROGEN, *Journal of Geophysical Research: Atmospheres*, 107, ACH 4–1–ACH 4–16, <https://doi.org/10.1029/2001JD001156>,
575 2002.
- Hersbach, H., Bell, B., Berrisford, P., Hirahara, S., Horányi, A., Muñoz-Sabater, J., Nicolas, J., Peubey, C., Radu, R., Schepers, D., Simmons, A., Soci, C., Abdalla, S., Abellan, X., Balsamo, G., Bechtold, P., Biavati, G., Bidlot, J., Bonavita, M., De Chiara, G., Dahlgren, P., Dee, D., Diamantakis, M., Dragani, R., Flemming, J., Forbes, R., Fuentes, M., Geer, A., Haimberger, L., Healy, S., Hogan, R. J., Hólm, E., Janisková, M., Keeley, S., Laloyaux, P., Lopez, P., Lupu, C., Radnoti, G., De Rosnay, P., Rozum, I., Vamborg, F., Villaume, S., and Thépaut,
580 J.: The ERA5 global reanalysis, *Quarterly Journal of the Royal Meteorological Society*, 146, 1999–2049, <https://doi.org/10.1002/qj.3803>, 2020.
- Hoesly, R. M., Smith, S. J., Feng, L., Klimont, Z., Janssens-Maenhout, G., Pitkanen, T., Seibert, J. J., Vu, L., Andres, R. J., Bolt, R. M., Bond, T. C., Dawidowski, L., Kholod, N., Kurokawa, J.-i., Li, M., Liu, L., Lu, Z., Moura, M. C. P., O'Rourke, P. R., and Zhang, Q.: Historical



- (1750–2014) anthropogenic emissions of reactive gases and aerosols from the Community Emissions Data System (CEDS), *Geoscientific Model Development*, 11, 369–408, <https://doi.org/10.5194/gmd-11-369-2018>, 2018.
- IEA: The Future of Hydrogen, Tech. rep., International Energy Agency, <https://www.iea.org/reports/the-future-of-hydrogen>, 2019.
- IEA: Global Hydrogen Review 2023, Tech. rep., International Energy Agency, <https://www.iea.org/reports/global-hydrogen-review-2023>, 2023.
- Inness, A., Ades, M., Agustí-Panareda, A., Barré, J., Benedictow, A., Blechschmidt, A.-M., Dominguez, J. J., Engelen, R., Eskes, H., Flemming, J., Huijnen, V., Jones, L., Kipling, Z., Massart, S., Parrington, M., Peuch, V.-H., Razinger, M., Remy, S., Schulz, M., and Suttie, M.: The CAMS reanalysis of atmospheric composition, *Atmospheric Chemistry and Physics*, 19, 3515–3556, <https://doi.org/10.5194/acp-19-3515-2019>, 2019.
- Jordan, A. and Steinberg, B.: Calibration of atmospheric hydrogen measurements, *Atmospheric Measurement Techniques*, 4, 509–521, <https://doi.org/10.5194/amt-4-509-2011>, 2011.
- Jordan, A., Moossen, H., Rothe, M., Brand, W., Heimann, M., Zaehle, S., and Rödenbeck, C.: Atmospheric flask sampling program of MPI-BGC, version 2024.1, <https://doi.org/10.17617/3.S3KHMS>, artwork Size: 9809288 Pages: 9809288, 2024.
- Krol, M., Houweling, S., Bregman, B., Van Den Broek, M., Segers, A., Van Velthoven, P., Peters, W., Dentener, F., and Bergamaschi, P.: The two-way nested global chemistry-transport zoom model TM5: algorithm and applications, *Atmospheric Chemistry and Physics*, 5, 417–432, <https://doi.org/10.5194/acp-5-417-2005>, 2005.
- Krummel, P., Langenfelds, R., Guerette, E., and Loh, Z.: Atmospheric H₂ at sites from the Commonwealth Scientific and Industrial Research Organisation (CSIRO) global monitoring network, https://doi.org/10.50849/WDCGG_H2_ALL_2025, 2025.
- McCarthy, M. C.: The hydrogen isotopic composition of water vapor entering the stratosphere inferred from high-precision measurements of CHD₃ and HD, *Journal of Geophysical Research*, 109, D07 304, <https://doi.org/10.1029/2003JD004003>, 2004.
- McKain, K., Sweeney, C., Crotwell, A., Crotwell, M., Higgs, J., Legard, T., Madronich, M., Miller, J., Moglia, E., Mund, J., Neff, D., Wolter, S., and NOAA Global Monitoring Laboratory: NOAA Global Greenhouse Gas Reference Network Flask-Air PFP Sample Measurements of CO₂, CH₄, CO, N₂O, H₂, SF₆ and isotopic ratios collected from aircraft vertical profiles, <https://doi.org/10.15138/39HR-9N34>, 2022.
- Montzka, S., Moore, F., and Sweeney, C.: Atmospheric Tomography Mission (ATom)ATom: L2 Measurements from the Programmable Flask Package (PFP) Whole Air Sampler, <https://doi.org/10.3334/ORNLDAAAC/1746>, artwork Size: 0 MB Medium: ICARTT Pages: 0 MB Version Number: 1, 2019.
- NOAA Global Monitoring Laboratory: Curve Fitting Methods Applied to Time Series (CCGCRV), <https://gml.noaa.gov/ccgg/mbl/crvfit/>, 2026.
- Novelli, P., Lang, P., Masarie, K., Hurst, D., Myers, R., and Elkins, J.: Molecular hydrogen in the troposphere: Global distribution and budget, *Journal of Geophysical Research*, 104, 30 427–30 444, <https://doi.org/10.1029/1999JD900788>, 1999.
- Ocko, I. B. and Hamburg, S. P.: Climate consequences of hydrogen emissions, *Atmospheric Chemistry and Physics*, 22, 9349–9368, <https://doi.org/10.5194/acp-22-9349-2022>, 2022.
- Ouyang, Z., Jackson, R. B., Saunio, M., Canadell, J. G., Zhao, Y., Morfopoulos, C., Krummel, P. B., Patra, P. K., Peters, G. P., Dennison, F., Gasser, T., Archibald, A. T., Arora, V., Baudoin, G., Chandra, N., Ciais, P., Davis, S. J., Feron, S., Guo, F., Hauglustaine, D., Jones, C. D., Jones, M. W., Kato, E., Kennedy, D., Knauer, J., Lienert, S., Lombardozzi, D., Melton, J. R., Nabel, J. E., O’Sullivan, M., Pétron, G., Poulter, B., Rogelj, J., Sandoval Calle, D., Smith, P., Suntharalingam, P., Tian, H., Wang, C., and Wiltshire, A.: The global hydrogen budget, *Nature*, 648, 616–624, <https://doi.org/10.1038/s41586-025-09806-1>, 2025.



- Paulot, F., Paynter, D., Naik, V., Malyshev, S., Menzel, R., and Horowitz, L. W.: Global modeling of hydrogen using GFDL-AM4.1: Sensitivity of soil removal and radiative forcing, *International Journal of Hydrogen Energy*, 46, 13 446–13 460, <https://doi.org/10.1016/j.ijhydene.2021.01.088>, 2021.
- Pieterse, G.: Modelling the global tropospheric molecular hydrogen cycle, Ph.D. thesis, Utrecht University, ISBN 978-94-6191-559-7, <https://dspace.library.uu.nl/handle/1874/259617>, 2013.
- 625 Pieterse, G., Krol, M. C., Batenburg, A. M., Steele, L. P., Krummel, P. B., Langenfelds, R. L., and Röckmann, T.: Global modelling of H₂ mixing ratios and isotopic compositions with the TM5 model, *Atmospheric Chemistry and Physics*, 11, 7001–7026, <https://doi.org/10.5194/acp-11-7001-2011>, 2011.
- Pieterse, G., Krol, M., Batenburg, A., Brenninkmeijer, C., Popa, E., O’Doherty, S., Grant, A., Steele, L., Krummel, P., Langenfelds, R., Wang, H., Vermeulen, A., Schmidt, M., Yver, C., Jordan, A., Engel, A., Fisher, R., Lowry, D., Nisbet, E., and Röckmann, T.: Reassessing the variability in atmospheric H₂ using the two-way nested TM5 model, *Journal of Geophysical Research*, <https://doi.org/10.1002/jgrd.50204>, 2013.
- 630 Pison, I., Bousquet, P., Chevallier, F., Szopa, S., and Hauglustaine, D.: Multi-species inversion of CH₄, CO and H₂ emissions from surface measurements, *Atmospheric Chemistry and Physics*, 9, 5281–5297, <https://doi.org/10.5194/acp-9-5281-2009>, 2009.
- 635 Price, H., Jaeglé, L., Rice, A., Quay, P., Novelli, P. C., and Gammon, R.: Global budget of molecular hydrogen and its deuterium content: Constraints from ground station, cruise, and aircraft observations, *Journal of Geophysical Research*, 112, D22 108, <https://doi.org/10.1029/2006JD008152>, 2007.
- Prinn, R., Weiss, R., Arduini, J., Choi, H., Engel, A., Fraser, P., Ganesan, A., Harth, C., Hermansen, O., Kim, J., Krummel, P., Loh, Z., Lunder, C., Maione, M., Manning, A., Mitrevski, B., Mühle, J., O’Doherty, S., Park, S., Pitt, J., Reimann, S., Rigby, M., Saito, T., Salameh, P., Schmidt, R., Simmonds, P., Stanley, K., Stavert, A., Steele, P., Vollmer, M., Wagenhäuser, T., Wang, H., Wenger, A., Western, L., Yao, B., Young, D., Zhou, L., and Zhu, L.: The dataset of in-situ measurements of chemically and radiatively important atmospheric gases from the Advanced Global Atmospheric Gas Experiment (AGAGE) and affiliated stations, <https://doi.org/10.60718/75D7-QE84>, 2025.
- 640 Pétron, G., Crotwell, A. M., Mund, J., Crotwell, M., Mefford, T., Thoning, K., Hall, B., Kitzis, D., Madronich, M., Moglia, E., Neff, D., Wolter, S., Jordan, A., Krummel, P., Langenfelds, R., and Patterson, J.: Atmospheric H₂ observations from the NOAA Cooperative Global Air Sampling Network, *Atmospheric Measurement Techniques*, 17, 4803–4823, <https://doi.org/10.5194/amt-17-4803-2024>, 2024.
- Rahn, T., Eiler, J. M., Boering, K. A., Wennberg, P. O., McCarthy, M. C., Tyler, S., Schauffler, S., Donnelly, S., and Atlas, E.: Extreme deuterium enrichment in stratospheric hydrogen and the global atmospheric budget of H₂, *Nature*, 424, 918–921, <https://doi.org/10.1038/nature01917>, 2003.
- Rhee, T. S., Brenninkmeijer, C. a. M., and Röckmann, T.: The overwhelming role of soils in the global atmospheric hydrogen cycle, *Atmospheric Chemistry and Physics*, 6, 1611–1625, <https://doi.org/10.5194/acp-6-1611-2006>, 2006.
- 650 Rodell, M., Houser, P. R., Jambor, U., Gottschalck, J., Mitchell, K., Meng, C.-J., Arsenault, K., Cosgrove, B., Radakovich, J., Bosilovich, M., Entin, J. K., Walker, J. P., Lohmann, D., and Toll, D.: The Global Land Data Assimilation System, *Bulletin of the American Meteorological Society*, 85, 381–394, <https://doi.org/10.1175/BAMS-85-3-381>, 2004.
- Röckmann, T., Rhee, T. S., and Engel, A.: Heavy hydrogen in the stratosphere, *Atmospheric Chemistry and Physics*, 3, 2015–2023, <https://doi.org/10.5194/acp-3-2015-2003>, 2003.
- 655 Sand, M., Skeie, R. B., Sandstad, M., Krishnan, S., Myhre, G., Bryant, H., Derwent, R., Hauglustaine, D., Paulot, F., Prather, M., and Stevenson, D.: A multi-model assessment of the Global Warming Potential of hydrogen, *Communications Earth & Environment*, 4, 1–12, <https://doi.org/10.1038/s43247-023-00857-8>, number: 1, 2023.



- Sand, M., Ocko, I. B., Sun, T., Skeie, R. B., Hauglustaine, D. A., Warwick, N. J., Stevenson, D. S., Paulot, F., Myhre, G., Archibald, A. T., Sandstad, M., Krishnan, S., and Prather, M.: Climate impacts of hydrogen emissions, *Nature Reviews Earth & Environment*, <https://doi.org/10.1038/s43017-026-00792-0>, 2026.
- Sander, S. P., Friedl, R. R., Ravishankara, A. R., Golden, D. M., Kolb, C. E., Kurylo, M. J., Molina, M. J., Moortgat, G. K., Keller-Rudek, H., Finlayson-Pitts, B. J., Wine, P. H., Huie, R. E., and Orkin, V. L.: Chemical Kinetics and Photochemical Data for Use in Atmospheric Studies: Evaluation No. 15, Tech. Rep. JPL Publication 06-2, Jet Propulsion Laboratory, California Institute of Technology, <https://jpldataeval.jpl.nasa.gov/>, 2006.
- Sanderson, M. G., Collins, W. J., Derwent, R. G., and Johnson, C. E.: Simulation of Global Hydrogen Levels Using a Lagrangian Three-Dimensional Model, *Journal of Atmospheric Chemistry*, 46, 15–28, <https://doi.org/10.1023/A:1024824223232>, 2003.
- Soulie, A., Granier, C., Darras, S., Zilbermann, N., Doumbia, T., Guevara, M., Jalkanen, J.-P., Keita, S., Liousse, C., Crippa, M., Guizzardi, D., Hoesly, R., and Smith, S. J.: Global anthropogenic emissions (CAM5-GLOB-ANT) for the Copernicus Atmosphere Monitoring Service simulations of air quality forecasts and reanalyses, *Earth System Science Data*, 16, 2261–2279, <https://doi.org/10.5194/essd-16-2261-2024>, 2024.
- Stuhl, F. and Niki, H.: Pulsed Vacuum-uv Photochemical Study of Reactions of OH with H₂, D₂, and CO Using a Resonance-Fluorescent Detection Method, *The Journal of Chemical Physics*, 57, 3671–3677, <https://doi.org/10.1063/1.1678825>, 1972.
- Sweeney, C., Karion, A., Wolter, S., Newberger, T., Guenther, D., Higgs, J. A., Andrews, A. E., Lang, P. M., Neff, D., Dlugokencky, E., Miller, J. B., Montzka, S. A., Miller, B. R., Masarie, K. A., Biraud, S. C., Novelli, P. C., Crotwell, M., Crotwell, A. M., Thoning, K., and Tans, P. P.: Seasonal climatology of CO₂ across North America from aircraft measurements in the NOAA/ESRL Global Greenhouse Gas Reference Network, *Journal of Geophysical Research: Atmospheres*, 120, 5155–5190, <https://doi.org/10.1002/2014JD022591>, 2015.
- Tardito Chaudhri, A. K. and Stevenson, D. S.: Soil deposition of atmospheric hydrogen constrained using planetary-scale observations, *Atmospheric Chemistry and Physics*, 25, 7369–7385, <https://doi.org/10.5194/acp-25-7369-2025>, 2025.
- Thompson, C. R., Wofsy, S. C., Prather, M. J., Newman, P. A., Hanisco, T. F., Ryerson, T. B., Fahey, D. W., Apel, E. C., Brock, C. A., Brune, W. H., Froyd, K., Katich, J. M., Nicely, J. M., Peischl, J., Ray, E., Veres, P. R., Wang, S., Allen, H. M., Asher, E., Bian, H., Blake, D., Bourgeois, I., Budney, J., Bui, T. P., Butler, A., Campuzano-Jost, P., Chang, C., Chin, M., Commane, R., Correa, G., Crouse, J. D., Daube, B., Dibb, J. E., DiGangi, J. P., Diskin, G. S., Dollner, M., Elkins, J. W., Fiore, A. M., Flynn, C. M., Guo, H., Hall, S. R., Hannun, R. A., Hills, A., Hintsa, E. J., Hodzic, A., Hornbrook, R. S., Huey, L. G., Jimenez, J. L., Keeling, R. F., Kim, M. J., Kupc, A., Lacey, F., Lait, L. R., Lamarque, J.-F., Liu, J., McKain, K., Meinardi, S., Miller, D. O., Montzka, S. A., Moore, F. L., Morgan, E. J., Murphy, D. M., Murray, L. T., Nault, B. A., Neuman, J. A., Nguyen, L., Gonzalez, Y., Rollins, A., Rosenlof, K., Sargent, M., Schill, G., Schwarz, J. P., Clair, J. M. S., Steenrod, S. D., Stephens, B. B., Strahan, S. E., Strode, S. A., Sweeney, C., Thames, A. B., Ullmann, K., Wagner, N., Weber, R., Weinzierl, B., Wennberg, P. O., Williamson, C. J., Wolfe, G. M., and Zeng, L.: The NASA Atmospheric Tomography (ATom) Mission: Imaging the Chemistry of the Global Atmosphere, *Bulletin of the American Meteorological Society*, 103, E761–E790, <https://doi.org/10.1175/BAMS-D-20-0315.1>, 2022.
- Thoning, K. W., Tans, P. P., and Komhyr, W. D.: Atmospheric carbon dioxide at Mauna Loa Observatory: 2. Analysis of the NOAA GMCC data, 1974–1985, *Journal of Geophysical Research: Atmospheres*, 94, 8549–8565, <https://doi.org/10.1029/JD094iD06p08549>, 1989.
- Tolk, L. F., Dolman, A. J., Meesters, A. G. C. A., and Peters, W.: A comparison of different inverse carbon flux estimation approaches for application on a regional domain, *Atmospheric Chemistry and Physics*, 11, 10349–10365, <https://doi.org/10.5194/acp-11-10349-2011>, 2011.



- Trapani, D., Marocco, P., Gandiglio, M., and Santarelli, M.: Hydrogen leakages across the supply chain: Current estimates and future scenarios, *International Journal of Hydrogen Energy*, 145, 1084–1095, <https://doi.org/10.1016/j.ijhydene.2025.06.103>, 2025.
- Van Der Laan-Luijkx, I. T., Van Der Velde, I. R., Van Der Veen, E., Tsuruta, A., Stanislawski, K., Babenhauerheide, A., Zhang, H. F., Liu, Y., He, W., Chen, H., Matarie, K. A., Krol, M. C., and Peters, W.: The CarbonTracker Data Assimilation Shell (CTDAS) v1.0: implementation and global carbon balance 2001–2015, *Geoscientific Model Development*, 10, 2785–2800, <https://doi.org/10.5194/gmd-10-2785-2017>, 2017.
- Van Der Werf, G. R., Randerson, J. T., Van Wees, D., Chen, Y., Giglio, L., Hall, J., Roland, V., Mu, M., Binte Shahid, S., Barsanti, K. C., Yokelson, R., and Morton, D. C.: Landscape fire emissions from the 5th version of the Global Fire Emissions Database (GFED5), *Scientific Data*, 12, 1870, <https://doi.org/10.1038/s41597-025-06127-w>, 2025.
- 705 Vollmer, M. K., Walter, S., Bond, S. W., Soltic, P., and Röckmann, T.: Molecular hydrogen (H_2) emissions and their isotopic signatures (H/D) from a motor vehicle: implications on atmospheric H_2 , *Atmospheric Chemistry and Physics*, 10, 5707–5718, <https://doi.org/10.5194/acp-10-5707-2010>, 2010.
- Walter, S., Kock, A., Steinhoff, T., Fiedler, B., Fietzek, P., Kaiser, J., Krol, M., Popa, M. E., Chen, Q., Tanhua, T., and Röckmann, T.: Isotopic evidence for biogenic molecular hydrogen production in the Atlantic Ocean, *Biogeosciences*, 13, 323–340, <https://doi.org/10.5194/bg-13-323-2016>, 2016.
- 710 Williams, J. and Van Noije, T.: On the upgrading of the modified Carbon Bond Mechanism IV for use in global Chemistry Transport Models, *Scientific Report WR-08-02*, KNMI, 2008.
- Williams, J. E., Boersma, K. F., Le Sager, P., and Verstraeten, W. W.: The high-resolution version of TM5-MP for optimized satellite retrievals: description and validation, *Geoscientific Model Development*, 10, 721–750, <https://doi.org/10.5194/gmd-10-721-2017>, 2017.
- 715 Wofsy, S., Daube, B., Jimenez-Pizarro, R., Kort, E., Pittman, J., Park, S., Commane, R., Xiang, B., Santoni, G., Jacob, D., Fisher, J., Pickett-Heaps, C., Wang, H., Wecht, K., Wang, Q., Stephens, B., Shertz, S., Watt, A., Romashkin, P., Campos, T., Haggerty, J., Cooper, W., Rogers, D., Beaton, S., Hendershot, R., Elkins, J., Fahey, D., Gao, R., Schwarz, J., Moore, F., Montzka, S., Perring, A., Hurst, D., Miller, B., Sweeney, C., Oltmans, S., Hints, E., Nance, D., Dutton, G., Watts, L., Spackman, J., Rosenlof, K., Ray, E., Hall, B., Zondlo, M., Diao, M., Keeling, R., Bent, J., Atlas, E., Lueb, R., and (Deceased), M. J. M.: HIPPO Combined Discrete Flask and GC Sample GHG, Halocarbon, and Hydrocarbon Data. Version 1.0, https://doi.org/10.3334/CDIAC/HIPPO_012, artwork Size: 1 data file, 4 ancillary/documentation files, 26 MiB Pages: 1 data file, 4 ancillary/documentation files, 26 MiB, 2017.
- 720 Wofsy, S., Afshar, S., Allen, H., Apel, E., Asher, E., Barletta, B., Bent, J., Bian, H., Biggs, B., Blake, D., Blake, N., Bourgeois, I., Brock, C., Brune, W., Budney, J., Bui, T., Butler, A., Campuzano-Jost, P., Chang, C., Chin, M., Commane, R., Correa, G., Crouse, J., Cullis, P. D., Daube, B., Day, D., Dean-Day, J., Dibb, J., DiGangi, J., Diskin, G., Dollner, M., Elkins, J., Erdesz, F., Fiore, A., Flynn, C., Froyd, K., Gesler, D., Hall, S., Hanisco, T., Hannun, R., Hills, A., Hints, E., Hoffman, A., Hornbrook, R., Huey, L., Hughes, S., Jimenez, J., Johnson, B., Katich, J., Keeling, R., Kim, M., Kupc, A., Lait, L., McKain, K., McLaughlin, R., Meinardi, S., Miller, D., Montzka, S., Moore, F., Morgan, E., Murphy, D., Murray, L., Nault, B., Neuman, J., Newman, P., Nicely, J., Pan, X., Paplawsky, W., Peischl, J., Prather, M., Price, D., Ray, E., Reeves, J., Richardson, M., Rollins, A., Rosenlof, K., Ryerson, T., Scheuer, E., Schill, G., Schroder, J., Schwarz, J., St.Clair, J., Steenrod, S., Stephens, B., Strobe, S., Sweeney, C., Tanner, D., Teng, A., Thames, A., Thompson, C., Ullmann, K., Veres, P., Wagner, N., Watt, A., Weber, R., Weinzierl, B., Wennberg, P., Williamson, C., Wilson, J., Wolfe, G., Woods, C., Zeng, L., and Vieznor, N.: Atmospheric Tomography Mission (ATom)ATom: Merged Atmospheric Chemistry, Trace Gases, and Aerosols, Version 2, <https://doi.org/10.3334/ORNLDAAAC/1925>, artwork Size: 0 MB Medium: netCDF-4 Pages: 0 MB Version Number: 2.0, 2021.
- 730



- Wofsy, S. C.: HIAPER Pole-to-Pole Observations (HIPPO): fine-grained, global-scale measurements of climatically important atmospheric gases and aerosols, *Philosophical Transactions of the Royal Society A: Mathematical, Physical and Engineering Sciences*, 369, 2073–
735 2086, <https://doi.org/10.1098/rsta.2010.0313>, 2011.
- Xiao, X., Prinn, R. G., Simmonds, P. G., Steele, L. P., Novelli, P. C., Huang, J., Langenfelds, R. L., O'Doherty, S., Krummel, P. B., Fraser, P. J., Porter, L. W., Weiss, R. F., Salameh, P., and Wang, R. H. J.: Optimal estimation of the soil uptake rate of molecular hydrogen from the Advanced Global Atmospheric Gases Experiment and other measurements, *Journal of Geophysical Research*, 112, D07 303, <https://doi.org/10.1029/2006JD007241>, 2007.
- 740 Yarwood, G., Rao, S., Way, R., Yocke, M., Whitten, G. Z., and Reyes, S.: Updates to the Carbon Bond chemical mechanism: CB05, Tech. rep., U.S. Environmental Protection Agency, 2005.
- Yashiro, H., Sudo, K., Yonemura, S., and Takigawa, M.: The impact of soil uptake on the global distribution of molecular hydrogen: chemical transport model simulation, *Atmospheric Chemistry and Physics*, 11, 6701–6719, <https://doi.org/10.5194/acp-11-6701-2011>, 2011.
- Yver, C. E., Pison, I. C., Fortems-Cheiney, A., Schmidt, M., Chevallier, F., Ramonet, M., Jordan, A., Søvde, O. A., Engel, A., Fisher, R. E.,
745 Lowry, D., Nisbet, E. G., Levin, I., Hammer, S., Necki, J., Bartyzel, J., Reimann, S., Vollmer, M. K., Steinbacher, M., Aalto, T., Maione, M., Arduini, J., O'Doherty, S., Grant, A., Sturges, W. T., Forster, G. L., Lunder, C. R., Privalov, V., Paramonova, N., Werner, A., and Bousquet, P.: A new estimation of the recent tropospheric molecular hydrogen budget using atmospheric observations and variational inversion, *Atmospheric Chemistry and Physics*, 11, 3375–3392, <https://doi.org/10.5194/acp-11-3375-2011>, 2011.